
FLOWR – FLOW MATCHING FOR STRUCTURE-AWARE *De Novo*, INTERACTION- AND FRAGMENT-BASED LIGAND GENERATION

Julian Cremer^{1,*,\dagger}, Ross Irwin^{2,3,*,\dagger}, Alessandro Tibo², Jon Paul Janet²,
Simon Olsson³, Djork-Arné Clevert¹

¹Machine Learning & Computational Sciences, Pfizer Worldwide R&D, Berlin, Germany

²Molecular AI, Discovery Sciences, R&D, AstraZeneca, Gothenburg, Sweden

³Department of Computer Science and Engineering,
Chalmers University of Technology and University of Gothenburg,
Gothenburg, Sweden

*Corresponding authors. Email: julian.cremer@pfizer.com, rossir@chalmers.se

^{\dagger}These authors contributed equally to this work.

ABSTRACT

We introduce FLOWR, a novel structure-based framework for the generation and optimization of three-dimensional ligands. FLOWR integrates continuous and categorical flow matching with equivariant optimal transport, enhanced by an efficient protein pocket conditioning. Alongside FLOWR, we present SPINDR, a thoroughly curated dataset comprising ligand-pocket co-crystal complexes specifically designed to address existing data quality issues. Empirical evaluations demonstrate that FLOWR surpasses current state-of-the-art diffusion- and flow-based methods in terms of PoseBusters-validity, pose accuracy, and interaction recovery, while offering a significant inference speedup, achieving up to 70-fold faster performance. In addition, we introduce FLOWR.MULTI, a highly accurate multi-purpose model allowing for the targeted sampling of novel ligands that adhere to predefined interaction profiles and chemical substructures for fragment-based design without the need of re-training or any re-sampling strategies. Collectively, our results indicate that FLOWR and FLOWR.MULTI represent a significant advancement in AI-driven structure-based drug design, substantially enhancing the reliability and applicability of *de novo*, interaction- and fragment-based ligand generation in real-world drug discovery settings.

1 Introduction

Structure-based drug discovery (SBDD) is an integrated computational and experimental approach that leverages the three-dimensional structures of biological macromolecules to guide the rational design and optimization of bioactive compounds. By analyzing protein or nucleic acid binding sites, SBDD aims to identify ligands capable of effectively modulating biological functions Anderson [2003, 2012]. Commonly employed techniques within this paradigm include molecular docking, virtual screening, and structure-guided ligand optimization Kitchen et al. [2004], Wang et al. [2015]. Despite notable successes, traditional SBDD methods face substantial challenges, such as the inherent complexity of molecular interactions, the vastness of chemical space, and difficulties in accurately predicting ligand binding poses and affinities Ferreira et al. [2015], Shoichet [2004].

Recent advances in deep learning have provided promising avenues to overcome these limitations. Classical computational methods, including molecular docking and virtual screening, typically rely on simplified approximations of molecular interactions and struggle to efficiently explore extensive chemical spaces. In contrast, data-driven deep learning approaches, particularly generative models, have demonstrated potential in capturing complex relationships inherent in distributions of experimentally determined ligand-protein complexes Jumper et al. [2021], Baek et al. [2021], Abramson et al. [2024].

Among generative modelling techniques, diffusion models have emerged as particularly promising tools for *de novo* ligand design. These models employ iterative stochastic processes to progressively refine molecular structures from

initial random noise into chemically valid conformations Hoogeboom et al. [2022], Vignac et al. [2023], Le et al. [2023]. By incorporating pocket-specific constraints during generation, diffusion models effectively capture the geometric and chemical subtleties of protein-ligand interactions, addressing the challenge of accurately predicting binding poses while generating diverse sets of novel ligands Luo et al. [2021], Peng et al. [2022], Guan et al. [2023], Schneuing et al. [2023], Le et al. [2023], Cremer et al. [2024].

Nevertheless, existing diffusion-based approaches are not without drawbacks. Their reliance on iterative stochastic sampling can result in molecules exhibiting strained conformations, uncommon substructures, and reduced drug-likeness Cremer et al. [2024]. Additionally, these methods typically suffer from prolonged sampling times compared to alternative generative frameworks Irwin et al. [2024].

Recently, generative flow matching models have emerged as an alternative paradigm, offering substantial improvements in generation efficiency Lipman et al. [2023]. Notably, flow matching approaches employing mini-batch Tong et al. [2024] and equivariant optimal transport Klein et al. [2023] have been proposed, with the latter demonstrating particular efficacy in molecular generation tasks Irwin et al. [2024].

Building upon these insights, we introduce FLOWR, a novel flow matching model specifically designed for the *de novo* generation of three-dimensional ligands explicitly conditioned on structural constraints. Our framework enables the efficient generation of ligands informed by the geometry of a protein pocket by using a dedicated pocket encoding scheme in contrast to prior works. In addition, we propose FLOWR.MULTI, a versatile extension capable of multi-purpose conditional generation. This model can efficiently and accurately generate ligands adhering to predefined interaction profiles between ligand atoms and pocket residues, and can design ligands around specific chemical substructures such as scaffolds and functional groups, facilitating scaffold elaboration, scaffold hopping, and fragment-based ligand design - all without requiring model retraining or computationally expensive stabilization techniques during inference as in prior work Schneuing et al. [2023].

However, the evaluation of novel SBDD methodologies remains challenging, primarily due to inherent data quality concerns and prevalent data leakage issues in widely utilized benchmark datasets Škrinjar et al. [2025], Durairaj et al. [2024]. In particular, the commonly employed CROSSDOCKED2020 dataset Francoeur et al. [2020] exhibits significant limitations for practical drug discovery applications, stemming from its reliance on rigid-pocket cross-docking protocols. Consequently, ligands are artificially constrained into co-crystallized binding pockets, causing models trained on such data to internalize biased, flawed, and unrealistic distributions of ligand-pocket interactions.

To address these critical issues, we introduce SPINDR, a high-quality benchmark dataset specifically developed for SBDD, derived from the recently presented PLINDER dataset Durairaj et al. [2024]. In constructing SPINDR, we implemented an extensive filtering and structural refinement pipeline designed to correct structural defects prevalent in existing datasets Wang et al. [2024], accurately infer protonation states, atomic-resolution protein-ligand interaction profiles, and minimize potential data leakage between training and test sets by maintaining the PLINDER dataset split.

In summary, we propose the FLOWR model that represents a significant advancement in both generative quality and computational efficiency. Additionally, our multi-purpose approach, FLOWR.MULTI, enables the generation of ligands conditioned on specific interaction profiles or chemical substructures, substantially increasing the proportion of ligands closely aligned with reference complexes and enhancing applicability in downstream tasks such as hit expansion, facilitating broader adoption in early-stage drug discovery. Finally, our SPINDR dataset establishes a new standard for training and evaluating 3D generative models, effectively addressing limitations—particularly regarding pose quality and data leakage—in currently available datasets.

2 The SPINDR Dataset

Modeling interactions between protein pockets and ligands has recently been gaining attention as a method for evaluating the quality of binding poses and designing better small molecule drug candidates Errington et al. [2024], Harris et al. [2023]. At the same time questions have been raised about the quality of existing benchmark datasets – PDBBind Wang et al. [2005] has been found to contain covalently bound ligands, missing atoms in pockets, and steric clashes between the pocket and the ligand Wang et al. [2024]. CROSSDOCKED2020 Francoeur et al. [2020], another commonly used dataset for pocket-conditioned ligand generative models, is based on the PDBBind General set and is also likely to share many of these structural defects. Additionally, questions have also been raised as to how well temporal data splits, which are commonly used to create benchmark test sets, are able to assess models’ abilities to generalise to unseen data since there are often close structural similarities between complexes in the training and test sets.

To address the issues of data quality and information leakage, and to provide rich, fine-grained information on the interactions between protein pockets and small molecule ligands, we present SPINDR (Small molecule Protein Interaction Dataset, Refined). Using the recently proposed PLINDER dataset Durairaj et al. [2024] as a starting point we

Table 1: An overview of the additional features provided by the SPINDR dataset compared to datasets commonly used for training generative models for structure-based drug design and docking tasks.

Dataset	Crystal Structure Complexes	Energy-Minimised Conformations	Explicit Hydrogens	Protein-Ligand Interactions
CROSSDOCKED	✗	✗	✗	✗
PDBBIND	✓	✗	✗	✗
SPINDR	✓	✓	✓	✓

apply an extensive filtering and processing pipeline to produce a refined set of high-quality structures. Specifically, to create the SPINDR dataset, we took the PLINDER dataset release 06/2024 (PLINDER version 2) and applied the following processing pipeline:

- Initial filtering.** We remove all PLINDER systems which contain more than one ligand or have more than one protein chain in the pocket. We then remove all systems where the ligand is marked as one or more of the following: ‘oligo’, ‘ion’, ‘cofactor’, ‘artifact’, ‘fragment’, ‘covalent’, or ‘other’.
- Structure refinement.** We use Schrodinger protein preparation wizard (which uses the OPLS 2005 force-field Banks et al. [2005]) to refine the structure of the remaining systems. These tools perform the following:
 - Add missing atoms to partially filled residues in the protein.
 - Convert some non-standard residue types to standard ones.
 - Assign protonation states to heavy atoms and add hydrogen atoms to both the protein and ligand.
 - Infer bonds and formal charges for both the protein and ligand.
 - Apply local energy minimisation to the protein-ligand complex.
- Infer protein-ligand interactions.** We use ProLIF Bouysset and Fiorucci [2021] to infer the interactions between the protein and ligand at an atomic resolution, creating a binary matrix of shape $N_{prot} \times N_{lig} \times |S|$, where N_{prot} is the number of atoms in the protein, N_{lig} is the number of atoms in the ligand, and S is the set of possible interaction types. We apply ProLIF with the default settings and infer all supported interaction types, $|S| = 13$.
- Quality filtering.** We apply a final filtering step and accumulate the processed systems into train, validation and testing splits. Here, we ensure that all systems contain RDKit-valid ligands. We also filter out any system which contains atoms other than $\{H, C, N, O, F, P, S, Cl, Se, Br\}$ and any system with fewer than 5 residues in the pocket. Additionally, we filter out all systems containing NAG ligands since we found these were highly overrepresented which would likely create an unwanted bias for generative models. We also filter out all systems derived from the PDB complex “1mvm” since it contains many small DNA fragments and was not originally filtered by PLINDER.
- Data deduplication.** Since existing datasets often contain significant structural redundancy, we also experiment with two data deduplication strategies – we present these in more detail in Appendix A. For the remainder of this paper, however, we make use of the non-deduplicated version of SPINDR.

Our final dataset contains 35,666 protein-ligand complexes, making SPINDR the largest dataset of high-quality, refined structures derived directly from crystallographic data. In Table 1 we compare some of the features of SPINDR to other commonly used dataset for SBDD and docking. Notably, in addition to the features in Table 1, we maintain the same data splits as PLINDER. The PLINDER splits were carefully selected to minimise data leakage between train and test sets and to ensure test systems were always of high-quality. This careful curation enables realistic assessment of models’ generalisability to unseen data, unlike many existing benchmarks which contain significant train-test data leakage Durairaj et al. [2024].

FLOWR – Structure-Aware Ligand Generation

We present FLOWR – a flow-based generative model for *de novo* ligand generation conditioned on a protein pocket and desired pocket-ligand features. We assume access to a dataset containing tuples of a ligand l , a protein pocket \mathcal{P} to which the ligand binds, and optionally a matrix $\mathcal{I} \in \mathbb{N}^{M \times N}$ of atomic protein-ligand features, where M and N refer to the number of atoms in the protein and ligand, respectively. In Fig 1 we show an overview of how our model generates novel ligands based on protein pocket and pocket-ligand feature conditioning.

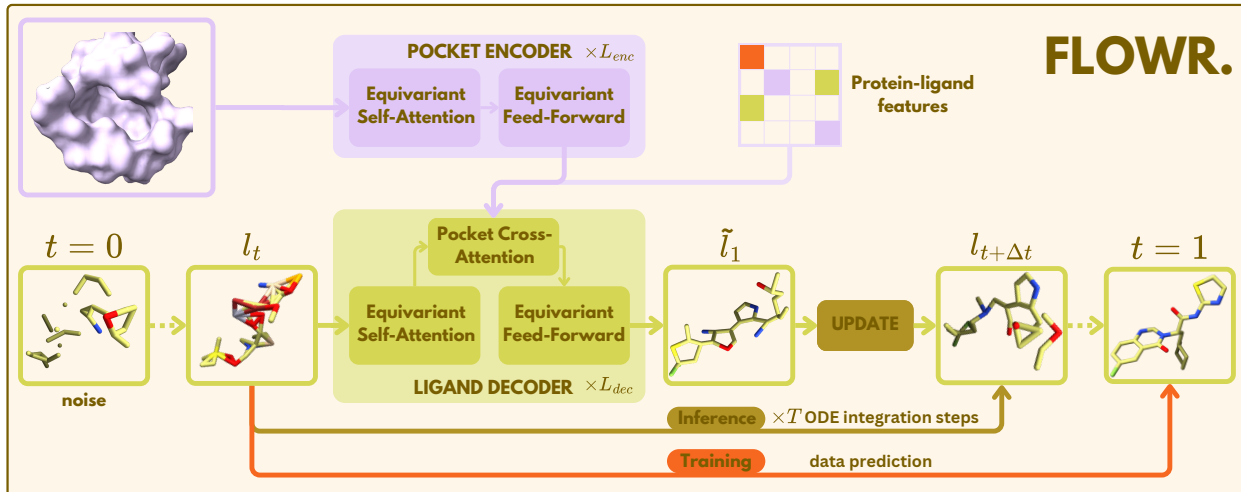


Figure 1: **Overview of FLOWR.** Schematical overview of the FLOWR model for 3D ligand generation. A protein pocket is encoded and passed, along with the noisy ligand l_t , into the ligand decoder, which is trained to produce a denoised ligand \tilde{l}_t . Optionally, a set of desired pocket-ligand features can be incorporated. A mixed continuous and categorical flow matching integration scheme is then used to push l_t towards the data distribution and generate a sample \tilde{l}_1 . The FLOWR model takes as input pocket coordinates along with atom, bond, and residue types, as well as ligand coordinates (with added noise), atom types, and bond types. Pocket features are processed through L_{enc} sequential blocks consisting of equivariant self-attention and equivariant feed-forward layers, resulting in a pocket encoding. This pocket encoding is subsequently integrated via equivariant cross-attention into L_{dec} blocks of equivariant self-attention that process ligand features. Finally, FLOWR outputs denoised ligand coordinates, atom types, bond types, and charges. During inference, the pocket encoding is computed only once and reused for all ligand generation steps.

We base the neural network architecture for FLOWR off the recently proposed SEMLAFLOW model Irwin et al. [2024], which achieves state-of-the-art results on unconditional 3D molecular generation tasks. SEMLAFLOW proposes SEMLA, an E(3)-equivariant architecture which includes a number of innovations making it significantly more efficient and scalable than previous models. We extend the SEMLA architecture to allow conditional generation by incorporating a separate pocket encoder and adding a cross attention module within the ligand decoder. This module follows a similar design to the attention module proposed by SEMLA, using a 2-layer MLP to produce attention scores. The module takes invariant and equivariant embeddings of \mathcal{P} , l_t and, optionally, \mathcal{I} , therefore allowing structural conditioning on the protein pocket and a set of desired protein-ligand features. We make use of the latent attention operation proposed in Irwin et al. [2024] to significantly increase the efficiency of this operation. Importantly, the pocket encoder module for FLOWR does not depend on t or l_t , meaning only one forward pass through the encoder is required when generating ligands, allowing the cost of encoding the pocket to be amortised over many ligands.

In addition to extending the architecture to allow conditional generation we also made improvements to various existing components within SEMLA, which we found to push the model’s performance and efficiency even further. We replace the equivariant feed-forward module in SEMLA with a version based on a gating component. Specifically, if the invariant and equivariant input features for the component for atom i are denoted by $\mathbf{h}_i \in \mathbb{R}^{d_{inv}}$ and $\mathbf{x}_i \in \mathbb{R}^{3 \times d_{equi}}$, respectively, then the output is given by $\mathbf{x}_i^{out} = \mathbf{W}_\theta^2 \hat{\mathbf{x}}_i$ where $\hat{\mathbf{x}}_i = \sigma(\Phi_\theta(\mathbf{h}_i, \|\mathbf{x}_i\|)) \odot \mathbf{W}_\theta^1 \mathbf{x}_i$. Here σ refers to an elementwise sigmoid function applied to invariant features, \odot denotes elementwise multiplication, $\mathbf{W}_\theta^1 \in \mathbb{R}^{d_{equi} \times d_{equi}}$ and $\mathbf{W}_\theta^2 \in \mathbb{R}^{d_{equi} \times d_{equi}}$ are both weight matrices, and Φ_θ is a two-layer MLP. We find this module is significantly faster than the equivariant feed-forward block used by SEMLA. Additionally, we pass bond embeddings into the self attention module on every layer, as opposed to only passing them to the first layer as proposed by SEMLA. We found this change led to improved validities of the generated molecules, while having only a very minor effect on inference time.

We parameterise FLOWR with a 4-layer pocket encoder with $d_{inv}^{enc} = 256$ and a 12-layer ligand decoder with $d_{inv}^{dec} = 384$. $d_{equi} = 64$ is the same for both encoder and decoder. For latent attention we use a latent size of 64 with 32 attention heads. An overview of the FLOWR architecture for ligand generation conditioned on a pocket is also shown in Figure 1.

FLOWR jointly models continuous (coordinates) and discrete (atom types, bond orders) molecular features. Training follows Irwin et al. [2024], using continuous flow matching Tong et al. [2024] for coordinates and discrete flow models Campbell et al. [2024] for categorical properties. Ligand formal charges are directly predicted. The model

learns to recover l_1 from l_t via $p_{1|t}^\theta(l_1|l_t, t; \mathcal{P}, \mathcal{I})$, minimizing mean-squared error for coordinates and cross-entropy for categorical features. Given \mathcal{P} and optionally \mathcal{I} , novel ligands are generated by iteratively refining an initial noisy ligand $l_0 \sim p_{\text{noise}}$. The model follows a learned vector field v_t^θ for continuous features and a discrete integration scheme for categorical attributes Campbell et al. [2024]. Full training and sampling details can be found in Appendix B.

2.1 FLOWR.MULTI: Multi-Purpose Training and Inference

In the following we propose FLOWR.MULTI—a multi-purpose model that simultaneously supports both *de novo* generation and any form of fragment-based sampling, like scaffold hopping, scaffold elaboration, fragment linking and fragment-based generation, which is highly relevant in hit expansion and lead optimization campaigns. As before, we consider a protein pocket \mathcal{P} and a protein-ligand feature matrix \mathcal{I} while assuming a (set of) pre-defined fragmentation(s) applied onto a ligand l . Let the ligand consist of N atoms with $\mathbf{l}_1 \in \mathbb{R}^{N \times 3}$ denoting its coordinates, and, for simplicity, assume that it is split into two fragments containing n_1 and n_2 atoms, respectively, with $n_1 + n_2 = N$. Thus, we have

$\mathbf{l}_{t_1 t_2} = \begin{pmatrix} \mathbf{l}_{t_1}^1 \\ \mathbf{l}_{t_2}^2 \end{pmatrix} \in \mathbb{R}^{(n_1+n_2) \times 3}$ with t_1 and t_2 sampled independently from a uniform distribution. Setting $\mathbf{t}_{12} = \begin{pmatrix} t_1 \\ t_2 \end{pmatrix}$,

the linear interpolation reads $\mathbf{l}_{t_1 t_2} = \mathbf{t}_{12} \odot \mathbf{l}_{t_1 t_2} + (\mathbf{1} - \mathbf{t}_{12}) \odot \mathbf{l}_{00} = \begin{pmatrix} t_1 \cdot \mathbf{l}_{t_1}^1 + (1 - t_1) \cdot \mathbf{l}_0^1 \\ t_2 \cdot \mathbf{l}_{t_2}^2 + (1 - t_2) \cdot \mathbf{l}_0^2 \end{pmatrix}$.

The goal is to learn a joint probability distribution $p_{1|t_1 t_2}^\theta(\mathbf{l}_1 | \mathbf{l}_{t_1 t_2}, \mathbf{t}_{12}; \mathcal{P}, \mathcal{I})$, from which at inference we sample

$\tilde{\mathbf{l}}_1 = \begin{pmatrix} \tilde{\mathbf{l}}_1^1 \\ \tilde{\mathbf{l}}_1^2 \end{pmatrix} \in \mathbb{R}^{N \times 3}$ to retrieve the joint vector field $f(\mathbf{l}_{t_1 t_2}, \mathbf{t}_{12}; \mathcal{P}, \mathcal{I}) = \tilde{\mathbf{l}}_1 - \mathbf{l}_{00}$.

Denoting the per-fragment step sizes by $\Delta t_1 = t_1 + s_1$ and $\Delta t_2 = t_2 + s_2$, where s_i is derived from the number of inference steps, and defining $\Delta \mathbf{t}_{12} = \begin{pmatrix} \Delta t_1 \\ \Delta t_2 \end{pmatrix}$, the Euler update step reads

$$\mathbf{l}_{t_1 + \Delta t_1 \ t_2 + \Delta t_2} = \mathbf{l}_{t_1 t_2} + \Delta \mathbf{t}_{12} \odot f(\mathbf{l}_{t_1 t_2}, \mathbf{t}_{12}; \mathcal{P}, \mathcal{I}) = \begin{pmatrix} \mathbf{l}_{t_1}^1 + \Delta t_1 \cdot (\tilde{\mathbf{l}}_1^1 - \mathbf{l}_0^1) \\ \mathbf{l}_{t_2}^2 + \Delta t_2 \cdot (\tilde{\mathbf{l}}_1^2 - \mathbf{l}_0^2) \end{pmatrix}.$$

Notably, when setting, e.g., $t_1 = 1$ and $\mathbf{l}_0^1 = \mathbf{l}_{t_1}^1 = \mathbf{l}_1^1$, we have $\Delta t_1 = 1$ as s_1 becomes 0 and the update becomes

$$\mathbf{l}_{1 \ t_2 + \Delta t_2} = \begin{pmatrix} \tilde{\mathbf{l}}_1^1 \\ \mathbf{l}_{t_2}^2 + \Delta t_2 \cdot (\tilde{\mathbf{l}}_1^2 - \mathbf{l}_0^2) \end{pmatrix}.$$

In this scenario, the atoms corresponding to $t_1 = 1$ remain fixed to be the predictions of the model at each inference step. Assuming the model has successfully learned the identity mapping $\tilde{\mathbf{l}}_1^1 = \mathbf{l}_1^1$ for the conditional distribution $p_{1|1 t_2}^\theta(\mathbf{l}_1 | \mathbf{l}_{1 t_2}, \begin{pmatrix} 1 \\ t_2 \end{pmatrix}; \mathcal{P}, \mathcal{I})$, this approach effectively resembles the concept of so-called inpainting. Originally proposed in computer vision Lugmayr et al. [2022], inpainting has already been adopted for molecular generation tasks Schneuing et al. [2023]. However, unlike the approach described in Schneuing et al. [2023], FLOWR.MULTI does not require re-sampling steps during inference (the authors report using 20 re-sampling steps). Furthermore, since FLOWR.MULTI is explicitly trained on a diverse set of inpainting tasks, we anticipate substantial improvements in both validity rates and generation efficiency and quality significantly increasing usefulness and downstream applicability.

3 Experiments and Results

We initially benchmark FLOWR against recent diffusion- and flow-based generative models using the widely adopted CROSSDOCKED2020 dataset Francoeur et al. [2020]. Despite its prevalence, we note that the CROSSDOCKED2020 dataset has several limitations. It is constructed via cross-docking procedures without adequately accounting for pocket flexibility, potentially misrepresenting the natural dynamics and interactions between ligands and their corresponding protein pockets. Moreover, from a practical application standpoint, the ligand chemical space coverage within CROSSDOCKED2020 is limited and notably biased towards non-drug-like or placeholder compounds.

Considering these drawbacks, we shift our primary evaluation to the proposed SPINDR dataset for the remainder of this study. We compare FLOWR directly with PILOT, a recently proposed diffusion-based model Cremer et al. [2024]. PILOT has demonstrated marked advancements in distribution learning and ligand quality metrics, outperforming earlier

Table 2: **Evaluation and comparison of FLOWR on CROSSDOCKED2020.** Benchmark comparison of the proposed FLOWR model against POCKET2MOL, TARGETDIFF, DIFFSBDD, PILOT and DRUGFLOW on the CROSSDOCKED2020 test dataset. We follow the conventions in this field and sample 100 ligands per test target, of which there are 100. We evaluate the most expressive metrics, namely PoseBusters-validity, GenBench3D strain energy, AutoDock-Vina scores and the Wasserstein distance of the generated ligands’ bond angles (BondA.W1) and bond lengths (BondL.W1) distributions relative to the test set. For all values, we report the mean across ligands and targets and the average standard deviation across targets. For all models, we ran all evaluations on the subset of RDKit-valid ligands.

MODEL	PB-VALID \uparrow	STRAIN \downarrow	VINA SCORE \downarrow	VINA SCORE ^{MIN} \downarrow	BONDA.W1 \downarrow	BONDL.W1 [10 ⁻²] \downarrow	SIZE	TIME (S) \downarrow
POCKET2MOL	0.76 \pm 0.39	147.22 \pm 61.41	-4.72 \pm 1.47	-5.80 \pm 1.26	2.04	0.66	17.04 \pm 4.11	2320 \pm 45
DIFFSBDD	0.38 \pm 0.46	519.03 \pm 251.32	-2.97 \pm 5.21	-4.71 \pm 3.30	7.00	0.51	24.85 \pm 8.94	160.31 \pm 73.30
TARGETDIFF	0.57 \pm 0.46	294.89 \pm 136.32	-5.20 \pm 1.79	-5.82 \pm 1.60	7.76	0.42	22.79 \pm 9.46	3228 \pm 121
DRUGFLOW	0.75 \pm 0.39	120.21 \pm 73.28	-5.66 \pm 1.78	-6.10 \pm 1.62	2.11	0.38	21.14 \pm 6.81	-
PILOT	0.83 \pm 0.33	110.48 \pm 87.47	-5.73 \pm 1.72	-6.21 \pm 1.65	1.75	0.33	22.58 \pm 9.77	295.42 \pm 117.35
FLOWR	0.92 \pm 0.22	87.83 \pm 74.30	-6.29 \pm 1.56	-6.48 \pm 1.45	0.96	0.27	22.28 \pm 9.78	12.05 \pm 8.01
TEST SET	0.95 \pm 0.21	75.62 \pm 57.29	-6.44 \pm 2.74	-6.46 \pm 2.61	-	-	22.75 \pm 9.90	-

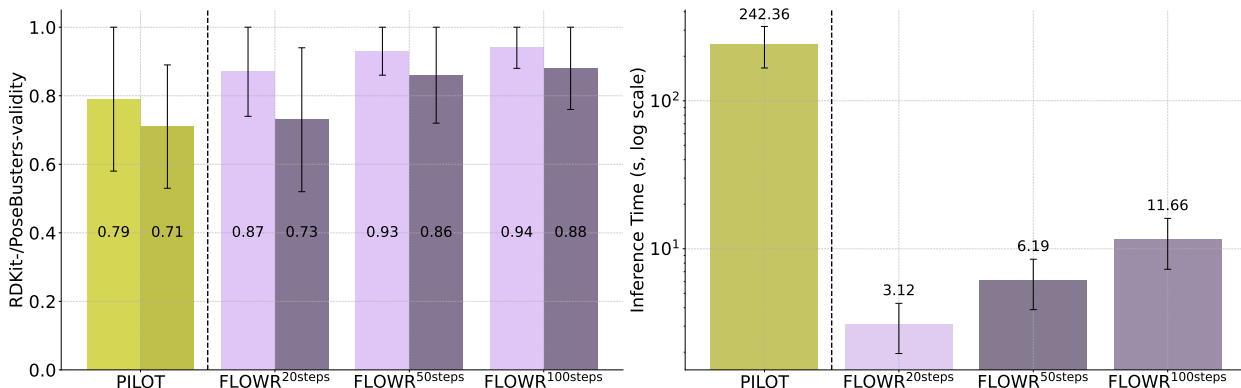


Figure 2: **Comparison of PILOT and FLOWR on validity and inference speed on SPINDR.** We compare PILOT and FLOWR in terms of RDKit- and PoseBusters-validity (left) and inference speed (right, log scale). Results for FLOWR are reported using three different inference step settings: 20, 50, and 100 steps. For each of the 225 targets in the SPINDR test set, we generate 100 ligands and compute the average validity scores and inference time per target. Note, both RDKit- and PoseBusters-validity are evaluated on the full set of generated ligands per target. Both models are evaluated using a single NVIDIA H100 GPU.

state-of-the-art methods, such as TARGETDIFF Guan et al. [2023] and DIFFSBDD Schneuing et al. [2023]. Our own evaluations on the CROSSDOCKED2020 dataset confirm PILOT’s robust performance, establishing it as the strongest competitor and thus the most relevant baseline against FLOWR. Given FLOWR’s improved computational efficiency and scalability, we further examine the effect of explicitly generating hydrogen atoms in ligands—a critical aspect often overlooked in previous studies despite the fundamental role of hydrogen bonding in protein-ligand interactions. Crucially, as the SPINDR dataset comes with pre-computed interaction profiles, we also compare PILOT and FLOWR in terms of interaction recovery, an important metric that helps to better assess ligand quality and distribution learning capabilities Errington et al. [2024]. We discuss the interactions within the SPINDR dataset more in Appendix C.

Lastly, we evaluate FLOWR.MULTI—specifically trained to generate ligands conditioned not only on protein pockets but also on predefined interaction profiles and chemical substructures—on two randomly selected targets from the SPINDR test set: 5YEA and 4MPE. A comprehensive evaluation of FLOWR.MULTI is provided in Appendix D.2.

3.1 Results

First, we compare our model against recently published generative methods on the commonly used CROSSDOCKED2020 dataset as a first benchmark. As can be seen in Tab 2, the proposed FLOWR model significantly outperforms all baseline methods (POCKET2MOL Peng et al. [2022], DIFFSBDD Schneuing et al. [2023], TARGETDIFF Guan et al. [2023], DRUGFLOW Schneuing et al. [2025], and PILOT Cremer et al. [2024]) across the evaluated metrics on the CROSSDOCKED2020 test dataset. Specifically, FLOWR achieves the highest PoseBusters-validity (0.92 \pm 0.22), lowest strain energy (87.83 \pm 74.30), best AutoDock-Vina scores (mean: -6.29 \pm 1.56, minimized: -6.48 \pm 1.45),

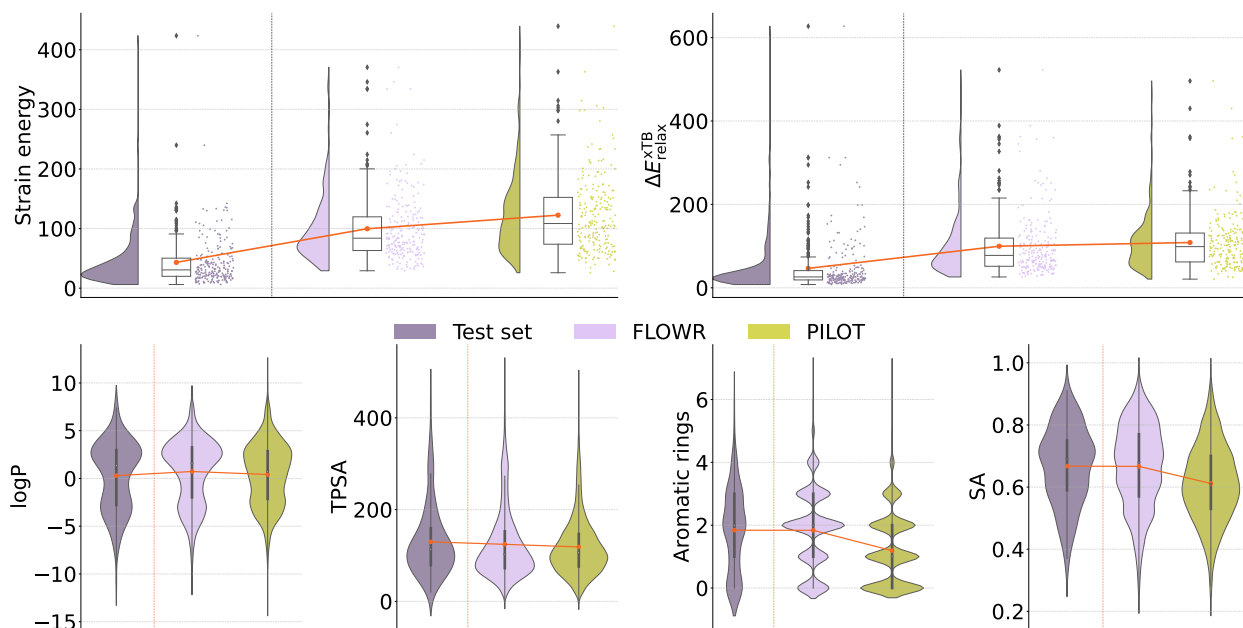


Figure 3: **Comparison of PILOT and FLOWR on molecular properties on SPINDR.** We compare PILOT and FLOWR in terms of strain energy (kcal/mol) and relaxation energy ($\Delta E_{\text{relax}}^{\text{XTB}}$ - kcal/mol) using GFN2-xTB with implicit solvation using the ALPB solvation model (top), and on logP, TPSA, number of aromatic rings and SA score (bottom). For each of the 225 targets in the SPINDR test set, we generate 100 ligands and compare the resulting distributions of both models. Red dots/lines highlight the respective mean values.

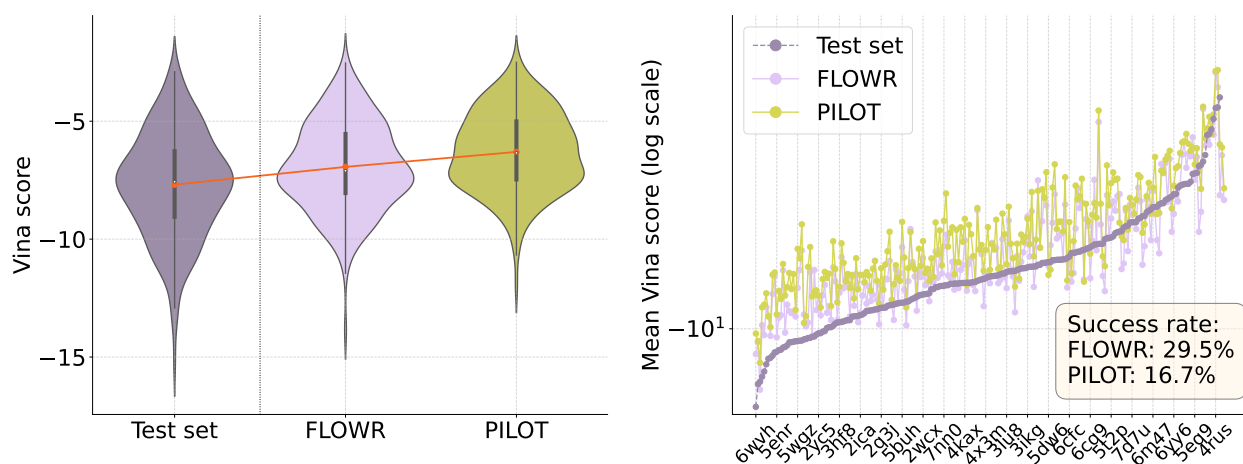


Figure 4: **Comparison of PILOT and FLOWR on AutoDock-Vina scores on SPINDR.** We compare PILOT and FLOWR in terms of Vina scores. For each of the 225 targets in the SPINDR test set, we generate 100 ligands and compare the resulting distributions of both models (left) and the mean Vina scores per target (right). Success rate denotes the mean number of ligands per target that outperform the respective reference ligand in terms of Vina score. Red dots/lines highlight the respective mean values.

and lowest Wasserstein distances for bond angles (0.96) and bond lengths (0.27). Additionally, FLOWR demonstrates significantly faster inference time (12.05 ± 8.01 seconds) compared to other methods. These results indicate that FLOWR generates ligand conformations closest to the test set distribution and with superior computational efficiency. We note that the second best model, PILOT, also shows significantly better results compared to all other methods, especially in terms of PoseBusters-validity (0.83 ± 0.33). Thus, we selected PILOT as our main competitor for the remaining of this study.

Table 3: **Evaluation and comparison of PILOT and FLOWR on SPINDR.** Benchmark comparison of the proposed FLOWR model against the PILOT model using the SPINDR test dataset, which consists of 225 targets. For FLOWR, results are reported for inference steps of 20, 50, and 100. For both models, 100 ligands were sampled per target. The evaluation includes strain energy calculated with GenBench3D and AutoDock-Vina scores (kcal/mol). Additionally, we report the Wasserstein distance of the generated ligands’ bond angles (BondA.W1), bond lengths (BondL.W1) and dihedral angles (DihedralW1) distributions relative to those in the SPINDR test set. Ligand sizes for all models are sampled uniformly with a -10%/+10% margin around the respective reference ligand size.

MODEL	STRAIN ENERGY ↓	VINA SCORE ↓	VINA SCORE ^{MIN} ↓	BONDA.W1 ↓	BONDL.W1 [10 ⁻²] ↓	DIHEDRALW1 ↓
PILOT	120.10 ± 71.61	-6.30 ± 0.96	-6.68 ± 1.07	1.82	0.42	5.52
FLOWR ^{20 STEPS}	134.70 ± 77.58	-6.61 ± 0.98	-6.92 ± 0.96	1.55	0.74	4.67
FLOWR ^{50 STEPS}	98.47 ± 56.64	-6.83 ± 0.93	-7.13 ± 0.93	1.18	0.51	4.04
FLOWR ^{100 STEPS}	90.05 ± 52.18	-6.93 ± 0.92	-7.22 ± 0.92	1.08	0.35	3.88
TEST SET	43.27 ± 41.85	-7.69 ± 2.00	-7.88 ± 2.00	-	-	-

Table 4: **Evaluation and comparison of PILOT and FLOWR on SPINDR with explicit hydrogens.** Benchmark comparison of the proposed FLOWR model against the PILOT model on the SPINDR test dataset with explicit hydrogens in training and inference. For both models, 100 ligands were sampled per target and evaluated in terms of strain energy, AutoDock-Vina scores (kcal/mol) and Wasserstein distances of generated ligands’ bond angle and bond length distributions relative to those in the test set.

MODEL	STRAIN ENERGY ↓	VINA SCORE ↓	VINA SCORE ^{MIN} ↓	BONDANGLESW1 ↓	BONDLENGTHSW1 [10 ⁻²] ↓
PILOT	53.07 ± 22.84	-5.00 ± 0.65	-5.50 ± 0.66	2.81	0.2
FLOWR ^{100 STEPS}	54.11 ± 33.36	-6.48 ± 0.87	-6.86 ± 0.87	0.82	0.1
TEST SET	43.27 ± 41.85	-7.69 ± 2.00	-7.88 ± 2.00	-	-

In Fig. 2, we compare PILOT and FLOWR trained on the SPINDR training dataset in terms of RDKit-validity, PoseBusters-validity (PB-validity), and inference speed on the SPINDR test set. Our results indicate that FLOWR generates ligands with significantly higher validity on average. While RDKit-validity is a 2D ligand-centric measure, the PoseBusters suite Buttenschoen et al. [2024] evaluates ligand conformations using well-established 3D ligand-pocket-based metrics, providing a more comprehensive assessment of pose accuracy. FLOWR achieves a substantial improvement over PILOT in both metrics, with an average RDKit-validity of 0.94 ± 0.24 vs. 0.79 ± 0.39 and an average PB-validity of 0.88 ± 0.21 vs. 0.71 ± 0.18 , respectively. Notably, FLOWR significantly improves inference speed, outperforming PILOT by a factor of 20 when using 100 inference steps, as shown in Fig. 2 (right). This efficiency gain is primarily attributed to FLOWR’s model architecture and the protein pocket encoder requiring only a single forward when integrating the vector field. In contrast, prior models Guan et al. [2023], Schneuing et al. [2023], Le et al. [2023], Cremer et al. [2024] often recompute protein pocket embeddings at every sampling step. Notably, the number of integration steps can be reduced as low as 20, achieving a 70-fold speed-up over PILOT while impacting model performance comparably little.

In Tab. 3 we compare PILOT and FLOWR in terms of strain energy (calculated using GenBench3D Baillif et al. [2024]), AutoDock-Vina score (used as an approximate measure of pose quality and binding affinity Eberhardt et al. [2021]), and their ability to generalize to the test set distribution based on Wasserstein distance measures for bond angles, bond lengths and dihedral angles following Vignac et al. [2023], Le et al. [2023], Cremer et al. [2024]. A more comprehensive overview of results is given in Tab. 7 in the Appendix. As flow matching allows for setting the number of inference steps, we also report the same results for different number of steps, namely 20, 50 and 100 (default).

In terms of strain energy values, FLOWR significantly outperforms PILOT (90.05 ± 52.18 vs. 120 ± 71.61). However, we note that, on average, the strain energies of generated ligands do not align well with those of the test set (43.27 ± 41.85), as illustrated in Fig. 3 (top left). We hypothesize that this discrepancy arises primarily from limited coverage of chemical and conformational space in the training data, due to the relatively low availability of co-crystal structures. Additionally, Fig. 3 (top right) shows the relaxation energy distribution of generated ligands calculated using the GFN2-xTB method Bannwarth et al. [2019] with implicit solvation using the ALPB model Ehlert et al. [2021] (46.37 ± 64.05 kcal/mol on the test set; 100.37 ± 59.85 for FLOWR vs. 107.89 ± 66.37 for PILOT). Another commonly reported metric in this context is the clash count between ligand and pocket atoms. Using PoseCheck Harris et al. [2023], we observe a clear improvement for FLOWR (5.25 ± 2.21) compared to the PILOT model (6.28 ± 2.61), with FLOWR more closely resembling the test set distribution (4.24).

FLOWR outperforms PILOT in docking assessments, suggesting a higher pose accuracy (-6.93 ± 0.92 vs. -6.30 ± 0.96). We use Vina’s scoring function with no re-docking applied, but also report the minimized Vina score, where local

energy minimization is applied to the ligand (-7.22 ± 0.92 vs. -6.68 ± 1.07). In Fig. 4 (left) we compare the Vina score distribution across targets and the mean Vina score per target (right, log-scale). As can be seen, FLOWR shows a 12.8% increase in success rate (number of ligands per target that are either equal or better than the reference with respect to Vina scoring) with an average success of 29.5%.

Additionally, we measure distribution learning capabilities in terms of bond angle and bond length Wasserstein distances to the test set. Here, FLOWR demonstrates significantly better generalization compared to PILOT with a mean bond angles distance of 1.08 vs. 1.82, mean bond lengths distance of 0.35 vs. 0.42 and mean dihedral angles distribution distance of 5.51 vs 3.45. We observe similar results when comparing both models on a set of relevant molecular properties like lipophilicity (logP), topological polar surface area (TPSA), number of aromatic rings and the synthesizability of generated molecules against the test set shown in Fig. 3 (bottom). While PILOT shows similar distributions for both logP and TPSA, it is significantly worse in reproducing the number of aromatic rings and similarly synthesizable compounds compared to the test set. In Fig. 14 in the Appendix, we provide additional results comparing FLOWR and PILOT on the SPINDR test set using key drug-likeness filters proposed by Walters et al. [1999]¹. These findings demonstrate that ligands generated by PILOT exhibit up to 40% lower pass-through rates compared to those generated by FLOWR, with FLOWR’s results aligning significantly more closely with the SPINDR test data.

In Tab. 4, we repeat the same experiments while incorporating explicit hydrogens in the ligands for both training and inference. Under these conditions, PILOT exhibits a clear decrease in performance, while FLOWR maintains comparable results. However, for both models validity drops significantly, with RDKit-validity decreasing to 0.64 ± 0.48 for FLOWR and 0.52 ± 0.50 for PILOT, while PB-validity declines to 0.60 ± 0.22 and 0.47 ± 0.14 , respectively. Since SPINDR provides limited coverage of both chemical and conformational space, we hypothesize that increasing data availability will alleviate this decline, particularly given the demonstrated learning efficiency of FLOWR.

Overall, the proposed FLOWR model consistently outperforms PILOT across all evaluated metrics, demonstrating significantly improved capability in modeling and generalizing ligand-pocket complex distributions. Specifically, we observe an average increase of approximately 15% in ligand and ligand-pocket validity metrics, along with substantially improved AutoDock-Vina scores, indicating higher-quality generated poses. Interestingly, using FLOWR with only 50 inference steps consistently yields better results and yields comparable or slightly worse results with 20 inference steps compared to the PILOT model with 500 steps. Thus, FLOWR achieves significant performance gains while reducing inference time by up to a factor of 70.

Nevertheless, there remains room for improvement, particularly in reducing strain energies of generated ligands. Additionally, accurately modeling ligand-pocket complexes with explicit hydrogens continues to be challenging, especially in scenarios with limited training data. We encourage the scientific community to evaluate generative models incorporating explicit hydrogen atoms as a novel and challenging benchmark in future research. In this context, the proposed SPINDR dataset represents a valuable resource, providing a robust and comprehensive benchmark for evaluating and comparing ligand generation models.

3.1.1 Interaction recovery

In SBDD, understanding how a ligand interacts with its target binding site at the atomic level is essential for optimizing potency, selectivity, and pharmacological properties Salentin et al. [2015], Jubb et al. [2016], Bouysset and Fiorucci [2021]. Ligand-pocket interactions—including hydrogen bonds, hydrophobic contacts, π - π and π -cation stacking, salt bridges, and electrostatic or van der Waals interactions—collectively determine binding affinity and specificity. Consequently, these protein-ligand interactions, or more precisely, the ligand’s binding pose, are crucial for assessing biological relevance and activity Errington et al. [2024]. To systematically identify such interactions, protein-ligand interaction fingerprints (PLIFs) are commonly employed Bouysset and Fiorucci [2021], Errington et al. [2024]. PLIFs encode key interaction features, including the interacting protein residue, interaction type, and optionally, the ligand atom involved Bouysset and Fiorucci [2021], Errington et al. [2024].

In contrast to previous studies, we closely investigate our proposed model’s capability to reproduce interactions observed in reference ligands. Figure 5 illustrates the distribution of interaction recovery rates for PILOT and FLOWR across the SPINDR test set targets, both with and without explicit hydrogen modeling, using the same sampling settings as before. We also report the success rate, defined as the proportion of RDKit- and PoseBusters-valid ligands for which interactions could be identified. As shown, FLOWR consistently outperforms PILOT (47.1% vs. 43.2%, with success rates of 90.4% vs. 75.5%), particularly when explicitly modeling hydrogens (42.5% vs. 26.5%, with success rates of 67.9% vs. 49.8%).

However, these results suggest that a purely *de novo* generation approach may be less suitable for targeted ligand generation tasks commonly employed in hit expansion and optimization campaigns. To address this, we propose

¹Inspired by this blog post by Pat Walters.

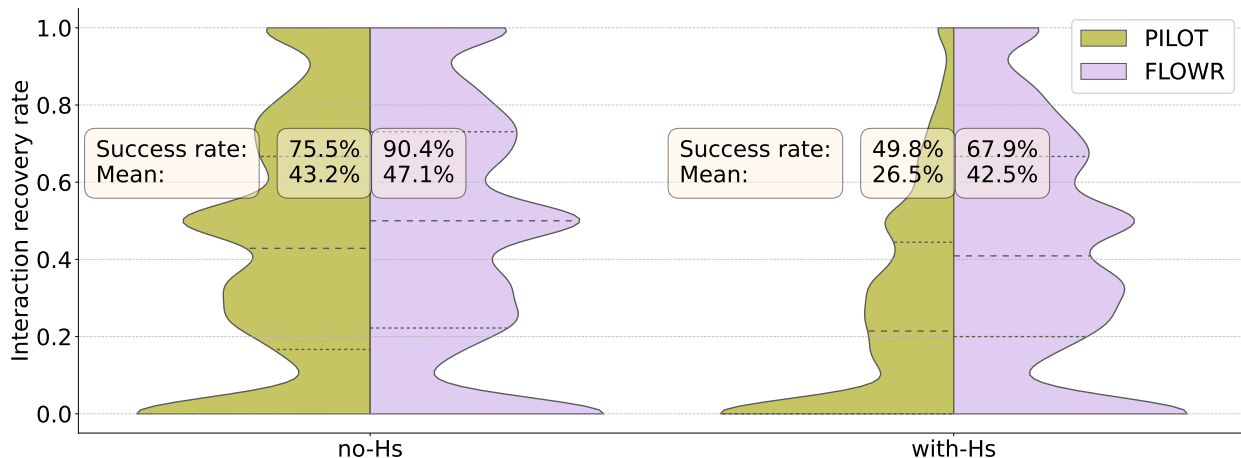


Figure 5: **Comparison of PILOT and FLOWR on interaction recovery on SPINDR.** We compare PILOT and FLOWR in terms of interaction recovery rates. Both models are either trained without explicit hydrogens (no-Hs) or with explicit hydrogens (with-Hs). The success rate is the percentage of ligands for which interaction fingerprints could be retrieved for 100 sampled ligands for every test set target. For calculating the interaction fingerprints we used PROLIF.

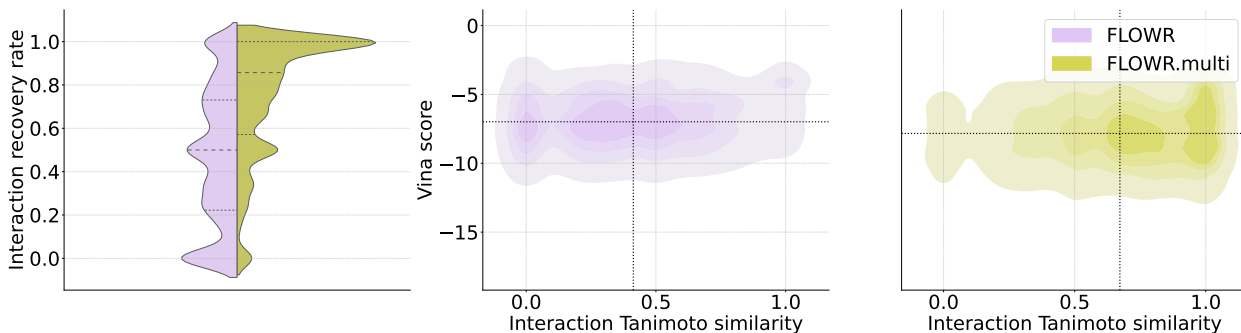


Figure 6: **Comparison of FLOWR and FLOWR.MULTI on interaction similarity and Vina scores on SPINDR.** We compare FLOWR (left) and FLOWR.MULTI (right) on interaction Tanimoto similarity and Vina scores for 100 sampled ligands per test set target. FLOWR.MULTI is jointly trained un- and interaction-conditionally via the proposed multi-purpose approach. The dotted lines indicate the respective mean values.

using FLOWR.MULTI (Sec. 2.1), a multi-purpose model capable of interaction-conditional generation. We present detailed results for this approach in the following section.

3.2 FLOWR.MULTI: Interaction-conditional generation

To improve interaction recovery, we propose to use FLOWR.MULTI with an interaction-based fragmentation for training and inference, which ensures that in inpainting-mode ligand atoms involved in pocket interactions are kept fixed. Let $\mathbf{X}_p = \{\mathbf{x}_{p,j} \in \mathbb{R}^3 : j = 1, \dots, n_p\}$ denote the 3D coordinates of the n_p pocket atoms, $\mathbf{X}_l = \{\mathbf{x}_{l,i} \in \mathbb{R}^3 : i = 1, \dots, n_l\}$ denote the ground-truth (native) 3D coordinates of the n_l ligand atoms, $I \in \{0, 1\}^{n_p \times n_l \times d_I}$ be an interaction tensor, where the entry $I_{j,i,k}$ indicates whether pocket atom j and ligand atom i participate in an interaction of type k (with d_I possible interaction channels). We define a binary mask $M \in \{0, 1\}^{n_l}$ by

$$M_i = \mathbb{I} \left\{ \sum_{j=1}^{n_p} \sum_{k=1}^{d_I} I_{j,i,k} > 0 \right\}, \quad i = 1, \dots, n_l. \quad (1)$$

which partitions the ligand atoms into a set of atoms for which we set $t_I = 1$ and $l_0^I = l_1^I$ and a set of atoms that are generated unconstrained, as described in Sec. 2.1.

Using FLOWR.MULTI, we achieve an average interaction recovery rate of 76.1%; the distribution compared to the FLOWR model is shown in Fig. 6 (left). Notably, despite the conditional generation process, the model maintains

Table 5: **Evaluation of FLOWR.MULTI on 5YEA and 4MPE.** Performance evaluation for interaction-, scaffold-, and functional group-conditional generation with FLOWR.MULTI on two randomly selected test targets with PDB-ID 5YEA and 4MPE, respectively. We report PoseBusters-validity (PB-validity) across 100 ligands per target, the mean Vina score (kcal/mol) as well as interaction recovery rate (PLIF recovery) and synthesizability score (SA score).

PROTEIN	METRIC	REFERENCE	FLOWR.MULTI ^{interact.-cond.}	FLOWR.MULTI ^{scaffold-cond.}	FLOWR.MULTI ^{f.group-cond.}
5YEA	PB-VALIDITY \uparrow	1.0	0.90	0.98	0.89
	VINA SCORE \downarrow	-9.57	-8.96	-8.71	-8.99
	VINA SCORE (TOP-10) \downarrow	-	-10.08	-10.16	-8.99
	PLIF RECOVERY RATE \uparrow	-	0.87	0.75	0.77
	SA SCORE \uparrow	0.82	0.77	0.82	0.76
4MPE	PB-VALIDITY \uparrow	1.0	0.95	1.0	0.92
	VINA SCORE \downarrow	-7.23	-6.80	-7.27	-6.41
	VINA SCORE (TOP-10) \downarrow	-	-7.54	-7.83	-7.15
	PLIF RECOVERY RATE \uparrow	-	0.79	0.53	0.89
	SA SCORE \uparrow	0.84	0.81	0.82	0.82

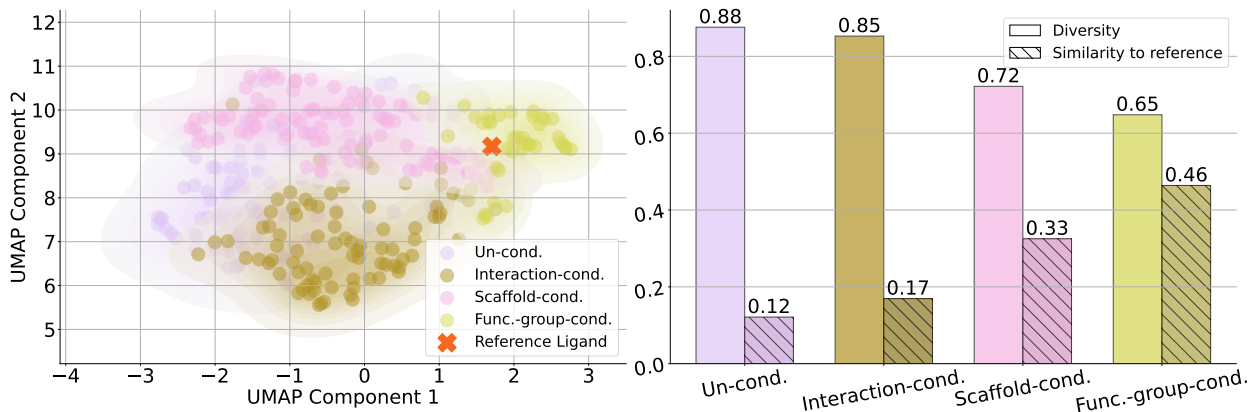


Figure 7: **Evaluation of chemical space coverage on 5YEA with FLOWR.MULTI.** Using the un-, interaction-, scaffold-, and functional group-conditional generation modes of FLOWR.MULTI, we sample 100 ligands each for a randomly selected target from the SPINDR test set, here the protein with PDB-ID 5YEA, visualize the chemical space coverage with respect to the reference (left), evaluate the average diversity of the sampled sets of ligands and their average similarity with the reference (right).

its ability to explore chemical space, achieving an average molecular diversity of 0.83 compared to 0.86 for FLOWR. As illustrated in Fig. 6 (right), FLOWR.MULTI also significantly improves predicted binding affinity, as indicated by a lower average Vina score (-7.18 vs. -6.93), while interaction Tanimoto similarity nearly doubles.

Thus, we observe that FLOWR.MULTI effectively generates ligands adhering to predefined interaction profiles, improving pose accuracy (as measured by Vina scoring) without substantially compromising chemical diversity or exploration compared to the purely *de novo* FLOWR model. For a more comprehensive overview of the performance of FLOWR.MULTI on the SPINDR test dataset for interaction-conditional and multi-purpose generation, we refer to Tab. 8 in the Appendix. In the next section, we further investigate the multi-purpose capabilities of FLOWR.MULTI in more details using two test set targets.

3.3 FLOWR.MULTI: Multi-purpose generation on 5YEA and 4MPE

To evaluate the multi-purpose generative capabilities of the FLOWR.MULTI model, we randomly selected two targets (PDB IDs: 5YEA and 4MPE) from the test set and generated ligands under three distinct conditions: interaction-conditional, scaffold-conditional, and functional group-conditional generation. Note that FLOWR.MULTI can also be applied to tasks such as fragment linking and fragment growing; however, for clarity, we leave the evaluation of these additional applications to future work.

The selected crystal structure 5YEA represents lipoprotein-associated phospholipase A2 (Lp-PLA2), a validated therapeutic target implicated in atherosclerosis, Alzheimer’s disease, and diabetic macular edema Liu et al. [2017]. Potent inhibitors has been found through fragment screening, molecular docking, and structure-guided optimization,

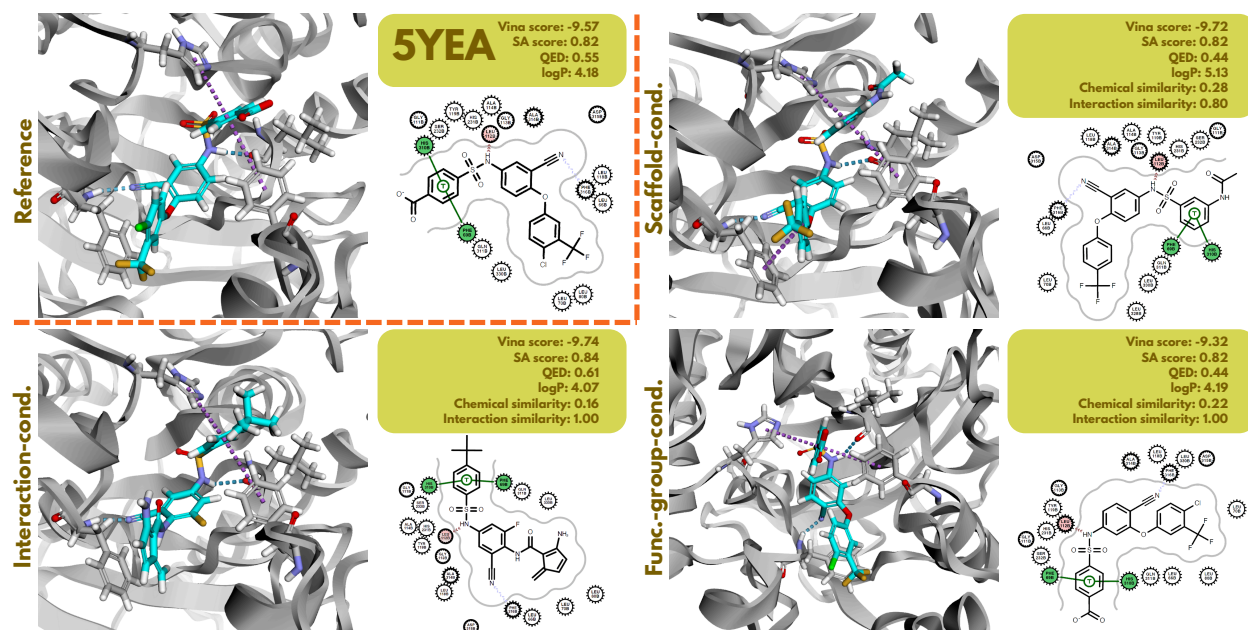


Figure 8: **Visualization of conditional generation on 5YEA with FLOWR.MULTI.** Using the interaction-, scaffold-, and functional group-conditional generation modes of FLOWR.MULTI, we sample 100 ligands for a randomly selected target from the SPINDR test set, here the protein with PDB-ID 5YEA. We then select three ligands at random and compare them to the reference compound based on Vina score, SA score, QED, logP, chemical similarity, and interaction similarity.

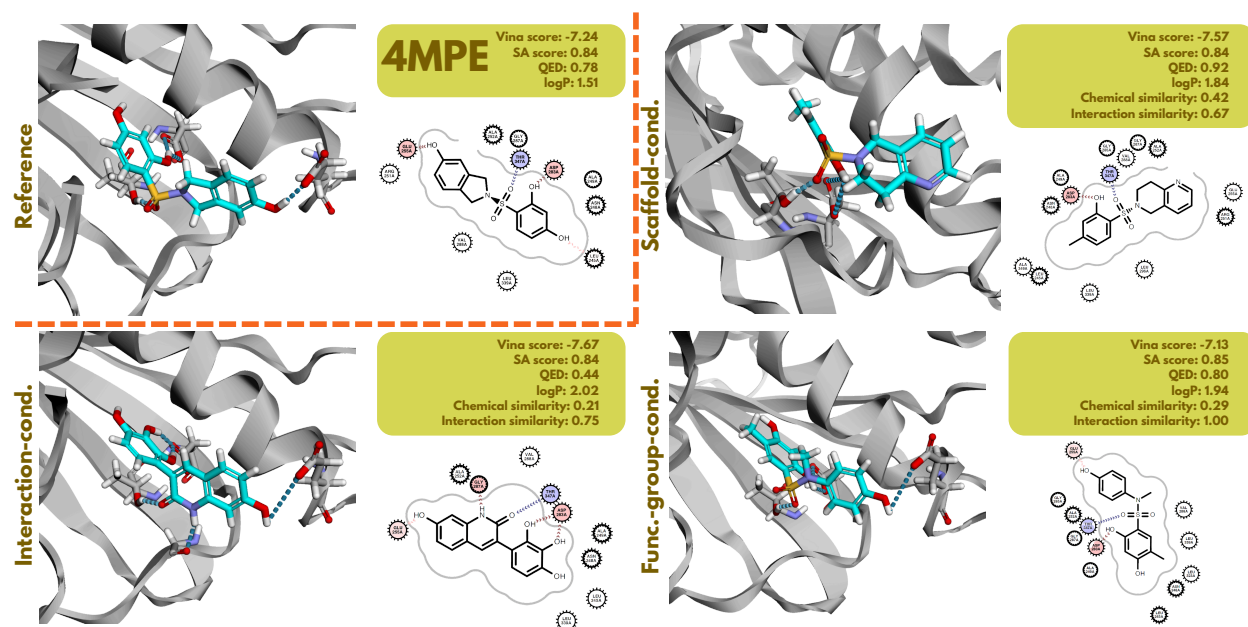


Figure 9: **Evaluation of conditional generation on 4MPE with FLOWR.MULTI** Using the interaction-, scaffold-, and functional group-conditional generation modes of FLOWR, we sample 100 ligands for a randomly selected target from the SPINDR test set, here 4MPE. We then select three ligands at random and compare them to the reference compound based on Vina score, SA score, QED, logP, chemical similarity, and interaction similarity.

achieving significant potency improvements from micromolar to single-digit nanomolar inhibitors Liu et al. [2017]. Given the proven effectiveness of structure-based approaches for this target, applying FLOWR.MULTI to Lp-PLA2 (5YEA) is particularly interesting. The other selected protein target, 4MPE, corresponds to pyruvate dehydrogenase

kinase (PDK), an enzyme family (isoforms 1–4) that negatively regulates mitochondrial pyruvate dehydrogenase complex activity through phosphorylation Tso et al. [2014]. PDK isoforms are clinically relevant, as their overexpression is associated with obesity, diabetes, heart failure, and cancer, making them attractive therapeutic targets. Previous works explored a structure-guided approach to design selective inhibitors targeting the conserved ATP-binding pocket of PDK isoforms, resulting in the potent inhibitor PS10 Tso et al. [2014], making it an interesting reference point for our FLOWR.MULTI model.

For each target and condition, we generated 100 ligands and compared the resulting ligand distributions to the respective reference ligand in terms of PoseBusters-validity, Vina docking score, interaction recovery rate, and synthetic accessibility. The results are summarized in Table 5. We consistently observe high PoseBusters-validity across targets, suggesting that FLOWR.MULTI effectively learned to generate accurate ligand poses independent of the conditioning mode. Although the mean Vina scores across generated ligands does not match those of the reference ligands, selecting the top-10 ligands based on Vina scores consistently yielded ligands with superior docking scores compared to the references (with slightly worse results for functional group-conditional generation). Interaction recovery rates are generally close to 1, indicating that the generated ligands closely reproduce the interaction profiles of the reference ligands. Finally, the mean SA scores, indicative of synthesizability, are consistently around or above 0.80, comparable to the reference ligands. This suggests that the generated ligands not only satisfy relevant physicochemical criteria but are also likely to be synthetically accessible. In Fig. 7 we show the chemical space coverage of generated ligands per generation mode, evaluate the sample diversity and the diversity towards the reference compound. Notably, we find a strong dependence of ligand diversity and reference similarity on the condition-mode. While in the *de novo* setting we get the most diverse set of ligands, as to be expected, the interaction-conditional also shows a strong chemical space coverage although interaction recovery is significantly enhanced reaching almost 90%. However, especially the functional-group-conditional setting allows for a close resemblance of the reference’s chemical space. This is interesting as this shows that practitioners can use different conditional setups of FLOWR.MULTI for controlled chemical space exploration. In Fig. 8 we visualize a randomly selected ligand for 5YEA per conditioning mode and compare to the reference ligand. More examples and visualizations also for 5YEA and 4MPE are provided in Appendix D.

3.4 Conclusion

In this work, we introduced FLOWR, a novel generative framework for structure-based *de novo* ligand design, integrating continuous and categorical flow matching with equivariant optimal transport and efficient protein pocket conditioning. Our empirical evaluations demonstrate that FLOWR significantly surpasses existing state-of-the-art diffusion- and flow-based methods across multiple critical metrics, including ligand validity, pose accuracy, interaction recovery, and inference speed. Specifically, FLOWR achieves up to 70-fold faster inference compared to diffusion-based methods.

Recognizing critical limitations in existing benchmark datasets, we also presented SPINDR, a rigorously curated dataset of ligand-pocket co-crystal complexes. By addressing prevalent structural defects, accurately inferring atomic-resolution interactions, protonation states and minimizing data leakage, SPINDR establishes a robust and realistic benchmark for evaluating generative models in structure-based drug discovery. Our results underscore the importance of high-quality datasets in accurately assessing model performance and generalization capabilities, and we encourage the adoption of SPINDR as a new standard for future research.

Furthermore, we introduced FLOWR.MULTI, a versatile extension enabling targeted ligand generation conditioned on predefined interaction profiles or chemical substructures. Our experiments illustrate that FLOWR.MULTI substantially enhances interaction recovery and ligand quality, making it particularly suitable for fragment-based drug design tasks such as scaffold hopping, scaffold elaboration, and fragment-based ligand optimization. We demonstrated the practical utility of FLOWR.MULTI in hit expansion scenarios on two randomly selected test set targets, highlighting its ability to generate ligands closely aligned with desired interaction patterns and chemical constraints.

Collectively, our contributions represent significant advancements in AI-driven structure-based drug discovery. By combining state-of-the-art generative modeling techniques with rigorous dataset curation, FLOWR and FLOWR.MULTI provide powerful, efficient, and reliable tools for ligand generation. These models are applicable across diverse drug discovery scenarios, including hit identification, scaffold elaboration, and fragment-based design. We envision the SPINDR dataset becoming a robust and challenging new standard for evaluating future SBDD models. Overall, we hope these developments will facilitate broader adoption of generative models in early-stage drug discovery.

References

- Josh Abramson, Jonas Adler, Jack Dunger, Richard Evans, Tim Green, Alexander Pritzel, Olaf Ronneberger, Lindsay Willmore, Andrew J. Ballard, Joshua Bambrick, Sebastian W. Bodenstein, David A. Evans, Chia-Chun Hung, Michael O'Neill, David Reiman, Kathryn Tunyasuvunakool, Zachary Wu, Akvilė Žemgulytė, Eirini Arvaniti, Charles Beattie, Ottavia Bertolli, Alex Bridgland, Alexey Cherepanov, Miles Congreve, Alexander I. Cowen-Rivers, Andrew Cowie, Michael Figurnov, Fabian B. Fuchs, Hannah Gladman, Rishub Jain, Yousuf A. Khan, Caroline M. R. Low, Kuba Perlin, Anna Potapenko, Pascal Savy, Sukhdeep Singh, Adrian Stecula, Ashok Thillaisundaram, Catherine Tong, Sergei Yakneen, Ellen D. Zhong, Michal Zielinski, Augustin Židek, Victor Bapst, Pushmeet Kohli, Max Jaderberg, Demis Hassabis, and John M. Jumper. Accurate structure prediction of biomolecular interactions with alphafold 3. *Nature*, 630(8016):493–500, Jun 2024. ISSN 1476-4687. doi: 10.1038/s41586-024-07487-w. URL <https://doi.org/10.1038/s41586-024-07487-w>.
- Michael S. Albergo and Eric Vanden-Eijnden. Building normalizing flows with stochastic interpolants, 2023. URL <https://arxiv.org/abs/2209.15571>.
- Amy C. Anderson. The process of structure-based drug design. *Chemistry & Biology*, 10(9):787–797, 2003. ISSN 1074-5521. doi: <https://doi.org/10.1016/j.chembiol.2003.09.002>. URL <https://www.sciencedirect.com/science/article/pii/S1074552103001947>.
- Amy C. Anderson. *Structure-Based Functional Design of Drugs: From Target to Lead Compound*, pages 359–366. Humana Press, Totowa, NJ, 2012. ISBN 978-1-60327-216-2. doi: 10.1007/978-1-60327-216-2_23. URL https://doi.org/10.1007/978-1-60327-216-2_23.
- Minkyung Baek, Frank DiMaio, Ivan Anishchenko, Justas Dauparas, Sergey Ovchinnikov, Gyu Rie Lee, Jue Wang, Qian Cong, Lisa N. Kinch, R. Dustin Schaeffer, Claudia Millán, Hahnbeom Park, Carson Adams, Caleb R. Glassman, Andy DeGiovanni, Jose H. Pereira, Andria V. Rodrigues, Alberdina A. van Dijk, Ana C. Ebrecht, Diederik J. Opperman, Theo Sagmeister, Christoph Buhlheller, Tea Pavkov-Keller, Manoj K. Rathinaswamy, Udit Dalwadi, Calvin K. Yip, John E. Burke, K. Christopher Garcia, Nick V. Grishin, Paul D. Adams, Randy J. Read, and David Baker. Accurate prediction of protein structures and interactions using a three-track neural network. *Science*, 373(6557):871–876, 2021. doi: 10.1126/science.abj8754. URL <https://www.science.org/doi/abs/10.1126/science.abj8754>.
- Benoit Baillif, Jason Cole, Patrick McCabe, and Andreas Bender. Benchmarking structure-based three-dimensional molecular generative models using genbench3d: ligand conformation quality matters, 2024. URL <https://arxiv.org/abs/2407.04424>.
- Jay L Banks, Hege S Beard, Yixiang Cao, Art E Cho, Wolfgang Damm, Ramy Farid, Anthony K Felts, Thomas A Halgren, Daniel T Mainz, Jon R Maple, et al. Integrated modeling program, applied chemical theory (impact). *Journal of computational chemistry*, 26(16):1752–1780, 2005.
- Christoph Bannwarth, Sebastian Ehlert, and Stefan Grimme. Gfn2-xtb—an accurate and broadly parametrized self-consistent tight-binding quantum chemical method with multipole electrostatics and density-dependent dispersion contributions. *Journal of Chemical Theory and Computation*, 15(3):1652–1671, Mar 2019. ISSN 1549-9618. doi: 10.1021/acs.jctc.8b01176. URL <https://doi.org/10.1021/acs.jctc.8b01176>.
- Cédric Bouysset and Sébastien Fiorucci. Prolif: a library to encode molecular interactions as fingerprints. *Journal of Cheminformatics*, 13(1):72, Sep 2021. ISSN 1758-2946. doi: 10.1186/s13321-021-00548-6. URL <https://doi.org/10.1186/s13321-021-00548-6>.
- Martin Buttenschoen, Garrett M. Morris, and Charlotte M. Deane. Posebusters: Ai-based docking methods fail to generate physically valid poses or generalise to novel sequences, 2024. URL <http://dx.doi.org/10.1039/D3SC04185A>.
- Andrew Campbell, Jason Yim, Regina Barzilay, Tom Rainforth, and Tommi Jaakkola. Generative flows on discrete state-spaces: Enabling multimodal flows with applications to protein co-design, 2024. URL <https://arxiv.org/abs/2402.04997>.
- Ting Chen, Ruixiang ZHANG, and Geoffrey Hinton. Analog bits: Generating discrete data using diffusion models with self-conditioning. In *The Eleventh International Conference on Learning Representations*, 2023. URL <https://openreview.net/forum?id=3itjR9QxFw>.
- Julian Cremer, Tuan Le, Frank Noé, Djork-Arné Clevert, and Kristof T Schütt. Pilot: Equivariant diffusion for pocket conditioned *de novo* ligand generation with multi-objective guidance via importance sampling. *arXiv preprint arXiv:2405.14925*, 2024.
- Janani Durairaj, Yusuf Adeshina, Zhonglin Cao, Xuejin Zhang, Vladas Oleinikovas, Thomas Duignan, Zachary McClure, Xavier Robin, Danny Kovtun, Emanuele Rossi, Guoqing Zhou, Srimukh Veccham, Clemens Isert, Yuxing

- Peng, Prabindh Sundareson, Mehmet Akdel, Gabriele Corso, Hannes Stärk, Zachary Carpenter, Michael Bronstein, Emine Kucukbenli, Torsten Schwede, and Luca Naef. Plinder: The protein-ligand interactions dataset and evaluation resource. *bioRxiv*, 2024. doi: 10.1101/2024.07.17.603955. URL <https://www.biorxiv.org/content/early/2024/07/17/2024.07.17.603955>.
- Jerome Eberhardt, Diogo Santos-Martins, Andreas F. Tillack, and Stefano Forli. Autodock vina 1.2.0: New docking methods, expanded force field, and python bindings. *Journal of Chemical Information and Modeling*, 61(8):3891–3898, Aug 2021. ISSN 1549-9596. doi: 10.1021/acs.jcim.1c00203. URL <https://doi.org/10.1021/acs.jcim.1c00203>.
- Sebastian Ehlert, Marcel Stahn, Sebastian Spicher, and Stefan Grimme. Robust and efficient implicit solvation model for fast semiempirical methods. *Journal of Chemical Theory and Computation*, 17(7):4250–4261, Jul 2021. ISSN 1549-9618. doi: 10.1021/acs.jctc.1c00471. URL <https://doi.org/10.1021/acs.jctc.1c00471>.
- David Errington, Constantin Schneider, Cédric Bouysset, and Frédéric A. Dreyer. Assessing interaction recovery of predicted protein-ligand poses, 2024. URL <https://arxiv.org/abs/2409.20227>.
- Peter Ertl and Ansgar Schuffenhauer. Estimation of synthetic accessibility score of drug-like molecules based on molecular complexity and fragment contributions. *Journal of cheminformatics*, 1(1):1–11, 2009.
- Leonardo G Ferreira, Ricardo N Dos Santos, Glaucius Oliva, and Adriano D Andricopulo. Molecular docking and structure-based drug design strategies. *Molecules*, 20(7):13384–13421, July 2015.
- Paul G. Francoeur, Tomohide Masuda, Jocelyn Sunseri, Andrew Jia, Richard B. Iovanisci, Ian Snyder, and David R. Koes. Three-dimensional convolutional neural networks and a cross-docked data set for structure-based drug design. *Journal of Chemical Information and Modeling*, 60(9):4200–4215, Sep 2020. ISSN 1549-9596. doi: 10.1021/acs.jcim.0c00411. URL <https://doi.org/10.1021/acs.jcim.0c00411>.
- Itai Gat, Tal Remez, Neta Shaul, Felix Kreuk, Ricky TQ Chen, Gabriel Synnaeve, Yossi Adi, and Yaron Lipman. Discrete flow matching. *arXiv preprint arXiv:2407.15595*, 2024.
- Jiaqi Guan, Wesley Wei Qian, Xingang Peng, Yufeng Su, Jian Peng, and Jianzhu Ma. 3d equivariant diffusion for target-aware molecule generation and affinity prediction. In *The Eleventh International Conference on Learning Representations*, 2023. URL <https://openreview.net/forum?id=kJqXEPXMsE0>.
- Charles Harris, Kieran Didi, Arian R Jamasb, Chaitanya K Joshi, Simon V Mathis, Pietro Lio, and Tom Blundell. Benchmarking generated poses: How rational is structure-based drug design with generative models? *arXiv preprint arXiv:2308.07413*, 2023.
- Emiel Hoogeboom, Víctor Garcia Satorras, Clément Vignac, and Max Welling. Equivariant diffusion for molecule generation in 3D. In Kamalika Chaudhuri, Stefanie Jegelka, Le Song, Csaba Szepesvari, Gang Niu, and Sivan Sabato, editors, *Proceedings of the 39th International Conference on Machine Learning*, volume 162 of *Proceedings of Machine Learning Research*, pages 8867–8887. PMLR, 17–23 Jul 2022. URL <https://proceedings.mlr.press/v162/hoogeboom22a.html>.
- Ross Irwin, Alessandro Tibo, Jon Paul Janet, and Simon Olsson. Efficient 3d molecular generation with flow matching and scale optimal transport, 2024. URL <https://arxiv.org/abs/2406.07266>.
- Harry C Jubb, Alicia P Higuero, Bernardo Ochoa-Montaño, Will R Pitt, David B Ascher, and Tom L Blundell. Arpeggio: A web server for calculating and visualising interatomic interactions in protein structures. *J Mol Biol*, 429(3):365–371, December 2016.
- John Jumper, Richard Evans, Alexander Pritzel, Tim Green, Michael Figurnov, Olaf Ronneberger, Kathryn Tunyasuvunakool, Russ Bates, Augustin Žídek, Anna Potapenko, Alex Bridgland, Clemens Meyer, Simon A. A. Kohl, Andrew J. Ballard, Andrew Cowie, Bernardino Romera-Paredes, Stanislav Nikolov, Rishub Jain, Jonas Adler, Trevor Back, Stig Petersen, David Reiman, Ellen Clancy, Michal Zielinski, Martin Steinegger, Michalina Pacholska, Tamas Berghammer, Sebastian Bodenstern, David Silver, Oriol Vinyals, Andrew W. Senior, Koray Kavukcuoglu, Pushmeet Kohli, and Demis Hassabis. Highly accurate protein structure prediction with alphafold. *Nature*, 596(7873):583–589, Aug 2021. ISSN 1476-4687. doi: 10.1038/s41586-021-03819-2. URL <https://doi.org/10.1038/s41586-021-03819-2>.
- Douglas B Kitchen, Hélène Decornez, John R Furr, and Jürgen Bajorath. Docking and scoring in virtual screening for drug discovery: methods and applications. *Nat Rev Drug Discov*, 3(11):935–949, November 2004.
- Leon Klein, Andreas Krämer, and Frank Noé. Equivariant flow matching, 2023. URL <https://arxiv.org/abs/2306.15030>.
- Tuan Le, Julian Cremer, Frank Noé, Djork-Arné Clevert, and Kristof Schütt. Navigating the design space of equivariant diffusion-based generative models for *de novo* 3d molecule generation, 2023.

- Yaron Lipman, Ricky T. Q. Chen, Heli Ben-Hamu, Maximilian Nickel, and Matt Le. Flow matching for generative modeling, 2023. URL <https://arxiv.org/abs/2210.02747>.
- Qiufeng Liu, Fubao Huang, Xiaojing Yuan, Kai Wang, Yi Zou, Jianhua Shen, and Yechun Xu. Structure-guided discovery of novel, potent, and orally bioavailable inhibitors of lipoprotein-associated phospholipase a2. *Journal of Medicinal Chemistry*, 60(24):10231–10244, 2017. doi: 10.1021/acs.jmedchem.7b01530. URL <https://doi.org/10.1021/acs.jmedchem.7b01530>. PMID: 29193967.
- Xingchao Liu, Chengyue Gong, and qiang liu. Flow straight and fast: Learning to generate and transfer data with rectified flow. In *The Eleventh International Conference on Learning Representations*, 2023. URL <https://openreview.net/forum?id=XVjTT1nw5z>.
- Andreas Lugmayr, Martin Danelljan, Andres Romero, Fisher Yu, Radu Timofte, and Luc Van Gool. Repaint: Inpainting using denoising diffusion probabilistic models, 2022. URL <https://arxiv.org/abs/2201.09865>.
- Shitong Luo, Jiaqi Guan, Jianzhu Ma, and Jian Peng. A 3d generative model for structure-based drug design. In M. Ranzato, A. Beygelzimer, Y. Dauphin, P.S. Liang, and J. Wortman Vaughan, editors, *Advances in Neural Information Processing Systems*, volume 34, pages 6229–6239. Curran Associates, Inc., 2021. URL https://proceedings.neurips.cc/paper_files/paper/2021/file/314450613369e0ee72d0da7f6fee773c-Paper.pdf.
- Xingang Peng, Shitong Luo, Jiaqi Guan, Qi Xie, Jian Peng, and Jianzhu Ma. Pocket2Mol: Efficient molecular sampling based on 3D protein pockets. In Kamalika Chaudhuri, Stefanie Jegelka, Le Song, Csaba Szepesvari, Gang Niu, and Sivan Sabato, editors, *Proceedings of the 39th International Conference on Machine Learning*, volume 162 of *Proceedings of Machine Learning Research*, pages 17644–17655. PMLR, 17–23 Jul 2022. URL <https://proceedings.mlr.press/v162/peng22b.html>.
- Sebastian Salentin, Sven Schreiber, V Joachim Haupt, Melissa F Adasme, and Michael Schroeder. PLIP: fully automated protein-ligand interaction profiler. *Nucleic Acids Res*, 43(W1):W443–7, April 2015.
- Arne Schneuing, Yuanqi Du, Charles Harris, Arian Jamasb, Ilia Igashov, Weitao Du, Tom Blundell, Pietro Lió, Carla Gomes, Max Welling, Michael Bronstein, and Bruno Correia. Structure-based drug design with equivariant diffusion models, 2023. URL <https://arxiv.org/abs/2210.13695>.
- Arne Schneuing, Ilia Igashov, Adrian W. Dobbstein, Thomas Castiglione, Michael M. Bronstein, and Bruno Correia. Multi-domain distribution learning for *de novo* drug design. In *The Thirteenth International Conference on Learning Representations*, 2025. URL <https://openreview.net/forum?id=g3VCIM94ke>.
- Brian K Shoichet. Virtual screening of chemical libraries. *Nature*, 432(7019):862–865, December 2004.
- Peter Škrinjar, Jérôme Eberhardt, Janani Durairaj, and Torsten Schwede. Have protein-ligand co-folding methods moved beyond memorisation? *bioRxiv*, 2025.
- Alexander Tong, Kilian FATRAS, Nikolay Malkin, Guillaume Huguet, Yanlei Zhang, Jarrid Rector-Brooks, Guy Wolf, and Yoshua Bengio. Improving and generalizing flow-based generative models with minibatch optimal transport. *Transactions on Machine Learning Research*, 2024. ISSN 2835-8856. URL <https://openreview.net/forum?id=CD9Snc73AW>.
- Shih-Chia Tso, Xiangbing Qi, Wen-Jun Gui, Cheng-Yang Wu, Jacinta L. Chuang, Ingrid Wernstedt-Asterholm, Lorraine K. Morlock, Kyle R. Owens, Philipp E. Scherer, Noelle S. Williams, Uttam K. Tambar, R. Max Wynn, and David T. Chuang. Structure-guided development of specific pyruvate dehydrogenase kinase inhibitors targeting the atp-binding pocket*. *Journal of Biological Chemistry*, 289(7):4432–4443, 2014. ISSN 0021-9258. doi: <https://doi.org/10.1074/jbc.M113.533885>. URL <https://www.sciencedirect.com/science/article/pii/S0021925820442243>.
- Clément Vignac, Nagham Osman, Laura Toni, and Pascal Frossard. Midi: Mixed graph and 3d denoising diffusion for molecule generation. In *Machine Learning and Knowledge Discovery in Databases: Research Track - European Conference, ECML PKDD 2023, Turin, Italy, September 18-22, 2023, Proceedings, Part II*, volume 14170 of *Lecture Notes in Computer Science*, pages 560–576. Springer, 2023. doi: 10.1007/978-3-031-43415-0_33. URL https://doi.org/10.1007/978-3-031-43415-0_33.
- W Patrick Walters, Ajay A Murcko, and Mark A Murcko. Recognizing molecules with drug-like properties. *Current Opinion in Chemical Biology*, 3(4):384–387, 1999. ISSN 1367-5931. doi: [https://doi.org/10.1016/S1367-5931\(99\)80058-1](https://doi.org/10.1016/S1367-5931(99)80058-1). URL <https://www.sciencedirect.com/science/article/pii/S1367593199800581>.
- Lingle Wang, Yujie Wu, Yuqing Deng, Byungchan Kim, Levi Pierce, Goran Krilov, Dmitry Lupyan, Shaughnessy Robinson, Markus K. Dahlgren, Jeremy Greenwood, Donna L. Romero, Craig Masse, Jennifer L. Knight, Thomas Steinbrecher, Thijs Beuming, Wolfgang Damm, Ed Harder, Woody Sherman, Mark Brewer, Ron Wester, Mark

Murcko, Leah Frye, Ramy Farid, Teng Lin, David L. Mobley, William L. Jorgensen, Bruce J. Berne, Richard A. Friesner, and Robert Abel. Accurate and reliable prediction of relative ligand binding potency in prospective drug discovery by way of a modern free-energy calculation protocol and force field. *Journal of the American Chemical Society*, 137(7):2695–2703, Feb 2015. ISSN 0002-7863. doi: 10.1021/ja512751q. URL <https://doi.org/10.1021/ja512751q>.

Renxiao Wang, Xueliang Fang, Yipin Lu, Chao-Yie Yang, and Shaomeng Wang. The pdbname database: methodologies and updates. *Journal of medicinal chemistry*, 48(12):4111–4119, 2005.

Yingze Wang, Kunyang Sun, Jie Li, Xingyi Guan, Oufan Zhang, Dorian Bagni, and Teresa Head-Gordon. Pdbname optimization to create a high-quality protein-ligand binding dataset for binding affinity prediction. *arXiv preprint arXiv:2411.01223*, 2024.

Appendix

A Additional Details on the SPINDR Dataset

Table 6: Sizes of train, validation and test dataset splits for the three proposed versions of the SPINDR dataset.

Dataset	Train Systems	Val Systems	Test Systems
SPINDR	35,373	68	225
SPINDR ^{RMSD}	24,885	68	225
SPINDR ^{RMSD-SEQID}	20,349	68	225

Like existing datasets of protein-ligand complexes, the SPINDR training set contains many redundant systems – systems which have significant structural similarity to another training system. Understanding the impact of this redundancy on model performance is a relatively unexplored topic but could have an important influence on the design of future datasets. We therefore apply two data deduplication strategies to SPINDR and report results on all three datasets. Deduplication is only applied to the training data and all models are evaluated identically.

Our first deduplication strategy works by creating groups of systems such that all systems within the group have identical ligands (based on their canonical SMILES after hydrogen atoms have been removed) and identical pockets atoms where the pocket coordinates are within an RMSD of 1.0 of some reference system for the group. We find that for system groups defined like this the distribution of RMSD values to the reference is very close to zero, so the choice of reference system and the RMSD threshold is not so important. In practice we iterate over all systems in the dataset, if a system cannot be added to an existing group a new group is created with this system as the group’s reference system. Once all systems in the training dataset have been grouped a single system is randomly selected from each group to form the deduplicated training set. We refer to this dataset as SPINDR^{RMSD}. We also explore an extension of this deduplication strategy which allows systems to be in the same group if the sequence identity between a query pocket and the pocket of the reference system for a group is greater than 90%. In this case the RMSD between the query and reference pockets is taken by comparing the coordinates only on matching residues. Again, once groups have been constructed, a single system is randomly sampled from each group to form the deduplicated training set. We refer to this dataset as SPINDR^{RMSD-SEQID}. The sizes of the three versions of the dataset are shown in Table 6.

A.1 SPINDR vs. CROSSDOCKED



Figure 10: Comparison of the SPINDR and CROSSDOCKED2020 datasets in terms of GFN2-xTB relaxation energies computed using the ALPB solvation model (left), as well as the proportion of unusual ring systems and potentially reactive functional groups identified according to two distinct substructure libraries, Dundee and LINT.

Fig. 10 compares the quality of ligands in the SPINDR dataset against those in the CROSSDOCKED2020 dataset, using three distinct metrics: relaxation energies using GFN2-xTB Bannwarth et al. [2019] together with the ALPB solvation

model Ehlert et al. [2021], frequency of odd ring systems, and presence of potentially reactive functional groups Walters et al. [1999]. Lower delta relaxation energies indicate higher conformational quality as ligands require less structural rearrangement upon binding. As illustrated, the SPINDR dataset exhibits significantly lower delta relaxation energies compared to CROSSDOCKED2020. Additionally, following Walters et al. [1999], odd ring systems are defined as ring structures that occur infrequently (fewer than 100 occurrences) within the ChEMBL database, indicating unusual or potentially problematic chemical motifs. Reactive functional groups were identified using standard medicinal chemistry filters, specifically the Dundee and LINT substructure collections. On all three metrics, SPINDR shows on average better values than the CROSSDOCKED2020 dataset.

B Additional Model Details

Here we provide a short introduction to the flow matching methods used in this paper and introduce the notation we will use for the full training and inference details below.

B.1 Flow Matching for Continuous Data

Flow matching Lipman et al. [2023], Albergo and Vanden-Eijnden [2023], Liu et al. [2023] is a generative model framework which aims to transport samples from an initial distribution p_0 to a target distribution p_1 by learning a vector field $v_t^\theta(x_t)$, which induces a time-dependent density p_t with p_0 and p_1 as endpoints. The key insight in flow matching is that such a vector field can be learned by firstly sampling data $x_1 \sim p_1(x_1)$, then sampling from a conditional probability path $x_t \sim p_{t|1}(x_t|x_1)$, which has an associated vector field $u_t(x_t|x_1)$, and finally regressing $v_t^\theta(x_t)$ against $u_t(x_t|x_1)$ Tong et al. [2024].

B.2 Discrete Flow Models

Frameworks for generating discrete sequences based on continuous-time markov chains (CTMC) have recently been proposed as an extension of flow matching to categorical data Campbell et al. [2024], Gat et al. [2024]. These methods work in a similar way to continuous flow matching by firstly defining a conditional probability path $p_{t|1}(\cdot|x_1)$ and then learning a data denoiser $p_{1|t}^\theta(\cdot|x_t)$ which is used during inference to push x_t towards the data distribution. The full details of the discrete flow model method we use in this paper can be found in Campbell et al. [2024].

B.3 Training and Inference

We train FLOWR to generate novel ligands conditioned on a given structure. Since 3D molecular graphs contain a mixture of continuous and categorical data types, FLOWR jointly generates continuous and discrete distributions. Our approach follows a similar setup to Irwin et al. [2024]. Specifically, we apply the continuous flow matching framework from Tong et al. [2024] to learn ligand coordinates, and the discrete flow models framework from Campbell et al. [2024] to learn atom types and bond orders. Ligand formal charges are not learned through a flow, but simply predicted by the model.

B.4 Model Training

Training proceeds by sampling ligand noise $l_0 \sim p_{\text{noise}}$, a ligand, pocket and interaction tuple $(l_1, \mathcal{P}, \mathcal{I}) \sim p_{\text{data}}$, and a time $t \in [0, 1]$. We use Gaussian noise for coordinates and uniform distributions for atom and bond types to create p_{noise} . We then sample a noisy ligand from the same conditional probability path $l_t \sim p_{t|1}(l_t|l_1)$ used in Irwin et al. [2024] and is defined as follows:

$$t \sim \text{Beta}(\alpha, \beta) \quad \mathbf{x}_t \sim \mathcal{N}(t\mathbf{x}_1 + (1-t)\mathbf{x}_0, \sigma^2) \quad (2)$$

$$\mathbf{a}_t \sim \text{Cat}(t\delta(\mathbf{a}_1) + (1-t)\frac{1}{|A|}) \quad \mathbf{b}_t \sim \text{Cat}(t\delta(\mathbf{b}_1) + (1-t)\frac{1}{|B|}) \quad (3)$$

Where A and B are the sets of possible values for atom types and bond orders, respectively, and $\delta(\cdot)$ is the one-hot encoding operation applied to each item in a sequence individually. We use values $\alpha = 2.0$, $\beta = 1.0$, and $\sigma = 0.2$ for all FLOWR models.

Following Vignac et al. [2023], Le et al. [2023], Cremer et al. [2024] we train FLOWR to predict l_1 directly by learning the distribution $p_{1|t}^\theta(l_1|l_t, \mathcal{P}, \mathcal{I})$. This leads to the same loss function as SEMLAFLOW Irwin et al. [2024] – we apply a mean-squared error loss for ligand coordinates and cross-entropy losses for atom types, bond orders and formal charges.

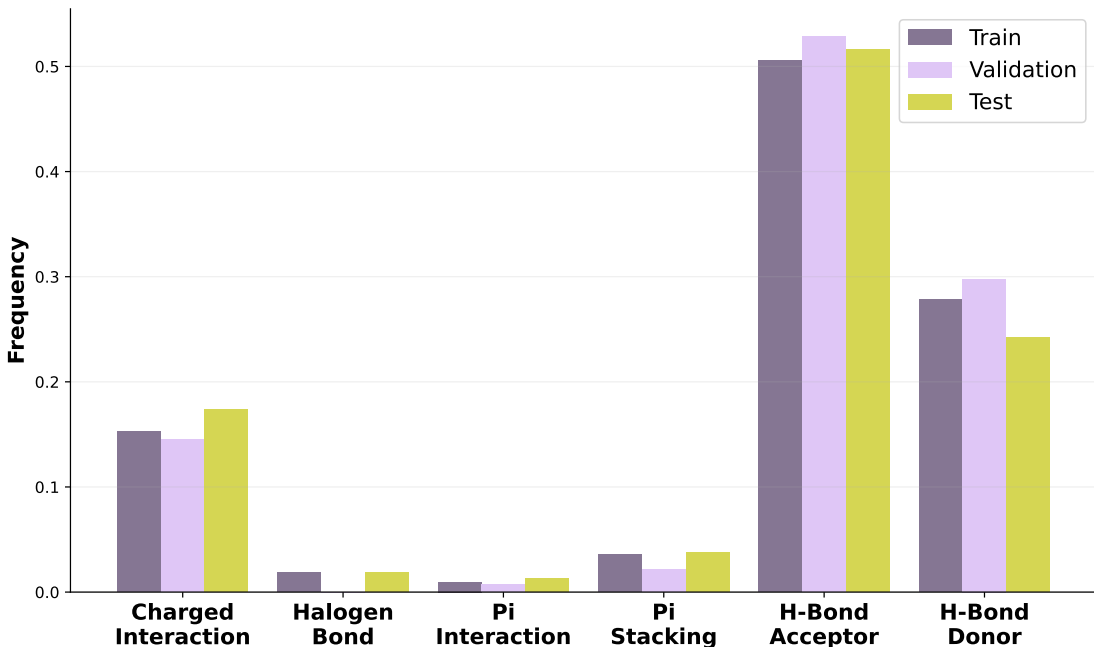


Figure 11: Distribution of interaction types on the train, validation and test sets of the SPINDR data that we considered in this work. Charged Interactions refers to either anionic or cationic interactions, and Pi Interactions refer to either cation-pi or pi-cation interactions. The SPINDR dataset contains all possible interactions supported by ProLIF, but we focus on the above interactions for conditional generation since they are the most applicable for small molecule binding.

In Appendix C we provide more information on how we handle the case where the model is conditioned on both \mathcal{P} and \mathcal{I} .

Additionally, during training we apply self-conditioning Chen et al. [2023] as a way of reusing the model’s previous prediction of l_1 and equivariant optimal transport Klein et al. [2023] to reduce the transport cost between p_{noise} and p_{data} . Full details of the training setup for self-conditioning and equivariant optimal transport can be found in Irwin et al. [2024].

B.5 Generating Novel Ligands

Given a protein pocket \mathcal{P} and, optionally, a desired interaction profile Ψ , we can generate samples from the learned data distribution by setting $l_t \leftarrow l_0$ where $l_0 \sim p_{\text{noise}}$ and pushing l_t toward the data distribution by following the learned vector field. Specifically, for molecular coordinates \mathbf{x}_t we follow the vector field $v_t^\theta(\mathbf{x}_t) = \frac{1}{1-t}(\tilde{\mathbf{x}}_1 - \mathbf{x}_t)$ where $\tilde{\mathbf{x}}_1$ is the coordinate component of $\tilde{l}_1 \sim p_{1|t}^\theta(l_1|l_t, \mathcal{P}, \mathcal{I})$. We then integrate the vector field using an Euler solver with step size Δt as follows: $\tilde{\mathbf{x}}_{t+\Delta t} = \mathbf{x}_t + \Delta t v_t^\theta(\mathbf{x}_t)$. We refer readers to Campbell et al. [2024] for full details on the integration scheme for discrete types.

Evaluation To maintain consistency across models, we used identical random seeds for training, inference, and data loading. Additionally, we applied the same sampling and evaluation scripts across all models. For each of the 225 test set targets, we generated 100 ligand samples using a standardized size sampling approach. Specifically, we determined native ligand sizes and applied a uniform sampling scheme, allowing for a size deviation of -25% to +10%. This procedure was performed using the same seed across all models to ensure direct comparability.

C Interactions

Following Errington et al. [2024], we consider a subset of interaction types in this work extracted using ProLIF Bouysset and Fiorucci [2021], including H-bonds (ligand acceptor and ligand donor), π - π stacking, halogen bonds (ligand donor), π -cation (ligand π / protein +), cation- π (ligand + / protein π), anionic (ligand - / protein +), and cationic (ligand + /

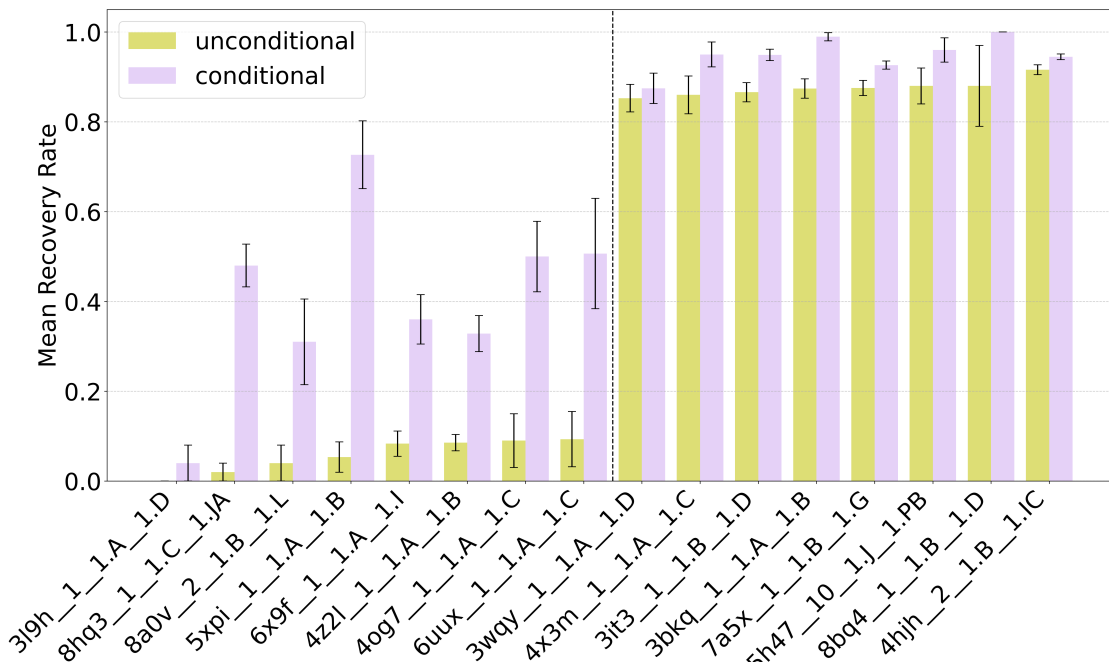


Figure 12: Comparison between FLOWR and FLOWR.MULTI. We identify eight targets with the lowest (left) and highest (right) average interaction recovery rates under the unconditional FLOWR model. For these selected targets, we compare the performance of the FLOWR.MULTI model to assess the impact of conditioning on pocket-ligand interactions.

protein-) interactions. The distribution of these interactions within the SPINDR dataset is shown in Fig. 11. Notably, interaction sparsity is high, with an average of 99.85% of ligand-protein atom pairs exhibiting no interactions.

C.1 Interactions per target

To better evaluate the effectiveness of the proposed interaction-conditional training and sampling, we compare FLOWR with FLOWR.MULTI models on a per-target basis. Given that the test set comprises 225 targets, visualizing results for all targets is impractical. Instead, we select M targets with the lowest and with the highest mean interaction recovery rates, as determined by the unconditional model, and compare the corresponding results obtained using the conditional model. This comparison is presented in Fig. 12. Notably, the conditional model consistently improves interaction recovery across targets where the unconditional model struggled to generate ligands with meaningful interactions. Additionally, it achieves significantly better results even for the top-performing targets, demonstrating that interaction-conditional generation effectively enhances ligand design with pre-specified interaction patterns.

Figure 13 presents an example of interaction profiling using the reference ligand of protein 6UUX alongside three randomly selected ligands generated by the interaction-conditional mode of FLOWR.MULTI model. The reference ligand forms two cationic interactions and one H-bond (ligand donor) interaction with ASP149, as well as two H-bond (ligand donor) interactions with ASP93. Notably, all of these interactions are successfully recovered in the generated ligands.

D Additional Experimental Results

Benchmarking newly proposed models and architectures in the context of structure-based drug design requires careful consideration of multiple evaluation aspects. In addition to the results presented in the main text, we provide a broader assessment using various metrics and evaluation settings in the following sections. Specifically, we evaluate the novelty of generated ligands with respect to the training set, as well as the average uniqueness and diversity among the 100 generated ligands per target. To ensure a comprehensive analysis, we consider both SMILES string- and ECFP4-based measures for uniqueness and diversity. Additionally, following Baillif et al. [2024], we extend this analysis to include conformer-based uniqueness and diversity. As indicators of drug-likeness, we report RDKit’s Quantitative Estimate of Drug-likeness (QED), the Synthetic Accessibility Score (SAScore) Ertl and Schuffenhauer [2009], molecular weight, logP values, and compliance with Lipinski’s Rule of Five. Furthermore, we assess model performance under a more

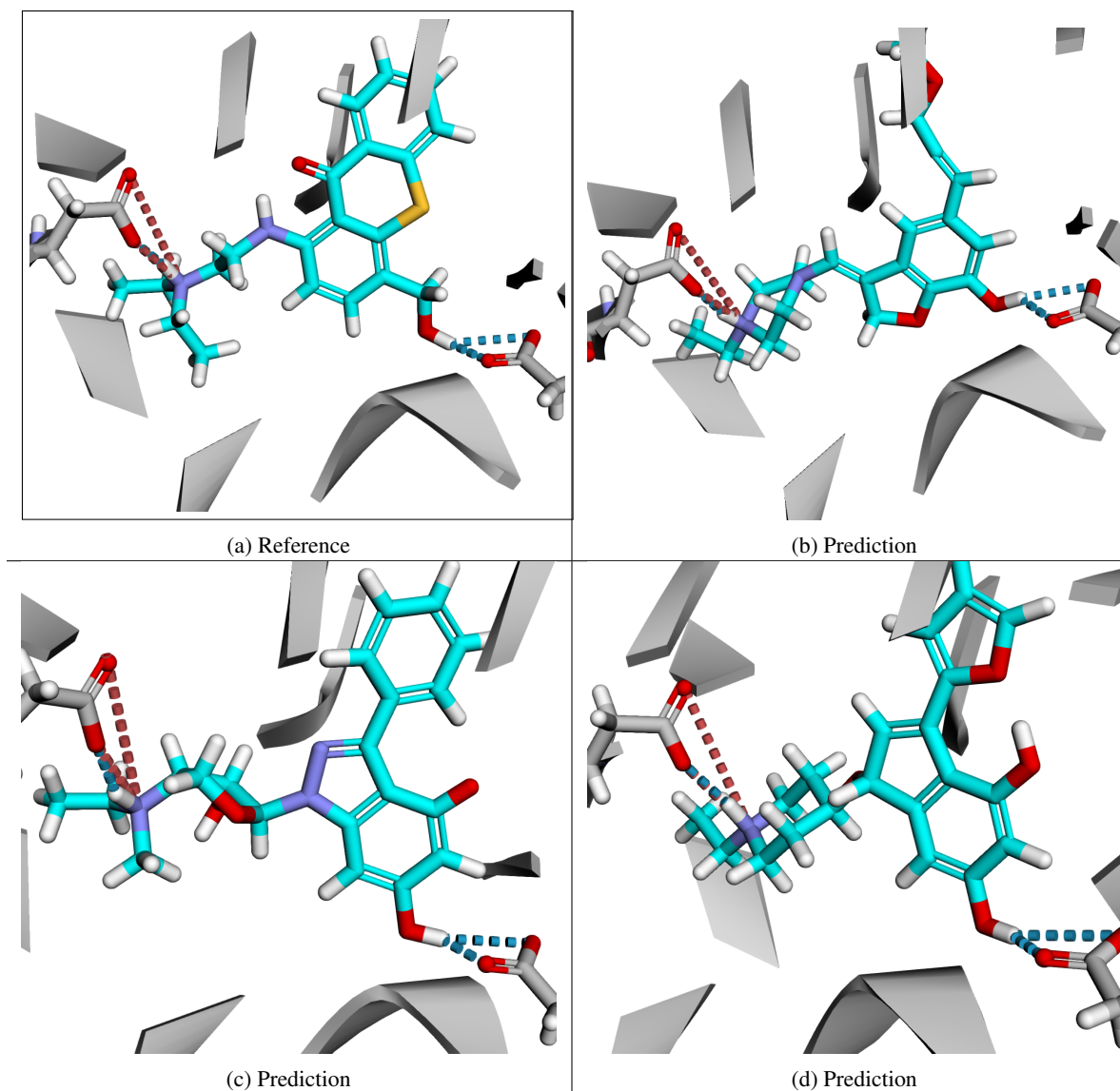


Figure 13: Comparison of reference and predicted ligands on their interaction profiles for the pocket of the protein with PDB id 6UUX sampled with FLOWR.MULTI.

restrictive ligand size setting, where ligand sizes are not sampled but fixed to match the sizes of the native ligands. This evaluation provides insights into how the models perform when constrained to a stricter ligand size distribution. Finally, we analyze the impact of reducing the number of inference steps in FLOWR, which allows for further reductions in inference time.

D.1 FLOWR vs. PILOT

In Tab. 7 we report the results comparing PILOT and FLOWR for both settings, without explicit and with explicit hydrogens in training and inference, respectively. On average, PILOT shows higher novelty, uniqueness and diversity values of generated ligands. However, in light of the significantly worse results across distribution and ligand-pocket centric metrics, it is likely that PILOT has a stronger tendency to hallucinate and thus generates physically less plausible, but more diverse structures with higher strains. Regarding RDKit-based ligand property metrics, both models show similar results, while FLOWR shows in general a higher overlap with the test set values indicating better distribution learning capabilities.

Table 7: Benchmark of the proposed FLOWR model against the recent state-of-the-art diffusion-based PILOT model on the SPINDR dataset. We report RDKit- and PoseBusters-validity of generated ligands, the GenBench3D strain energy and the AutoDock-Vina score. We also state the Wasserstein distance of generated ligands for the bond angles and bond lengths distribution to the SPINDR test set. Novelty, uniqueness and diversity measure the capability of the model to explore the chemical space both in 2D and 3D. RDKit’s QED evaluation, SAScore, the molecular weight as well as the logP values evaluate drug-likeness of generated ligands. All presented values are mean values taken for 100 sampled ligands per test set target. The test dataset comprises 225 test set targets. Ligand sizes were drawn from a uniform distribution around the ground truth ligand size allowing for a deviation of -10% and + 10% with the same random seed for all models. Note, both RDKit- and PoseBusters-validity are evaluated on the raw generated set of 100 ligands per target. All other metrics are calculated on the subset of RDKit-valid ligands.

METRIC	TEST SET	PILOT ^{NO-HS}	PILOT ^{WITH-HS}	FLOWR ^{NO-HS}	FLOWR ^{WITH-HS}
RDKIT-VALIDITY	1.00 ± 0.00	0.79 ± 0.39	0.52 ± 0.50	0.94 ± 0.24	0.64 ± 0.48
PB-VALIDITY	0.99 ± 0.02	0.71 ± 0.18	0.47 ± 0.14	0.88 ± 0.21	0.60 ± 0.22
STRAIN ENERGY	43.27 ± 41.85	120.10 ± 71.61	53.07 ± 22.84	90.05 ± 52.18	54.11 ± 33.36
VINA SCORE	-7.69 ± 2.00	-6.30 ± 0.96	-5.00 ± 0.65	-6.93 ± 0.92	-6.48 ± 0.87
VINA SCORE (MINIMIZED)	-7.88 ± 2.00	-6.68 ± 1.07	-5.50 ± 0.66	-7.22 ± 0.92	-6.86 ± 0.87
BONDANGLESWI	-	1.82	2.81	1.08	0.82
BONDLENGTHSWI [10 ⁻²]	-	0.42	0.10	0.35	0.11
NOVELTY	1.00 ± 0.00	0.99 ± 0.10	1.00 ± 0.00	0.94 ± 0.23	1.00 ± 0.00
UNIQUENESS2D	0.92 ± 0.10	0.99 ± 0.05	1.00 ± 0.02	0.94 ± 0.13	0.97 ± 0.07
UNIQUENESS3D	-	0.66 ± 0.20	0.59 ± 0.19	0.50 ± 0.20	0.55 ± 0.17
DIVERSITY2D	0.92 ± 0.04	0.89 ± 0.03	0.90 ± 0.02	0.86 ± 0.05	0.87 ± 0.06
DIVERSITY3D	-	0.25 ± 0.13	0.13 ± 0.19	0.21 ± 0.12	0.18 ± 0.11
SA	0.66 ± 0.12	0.63 ± 0.12	0.64 ± 0.10	0.67 ± 0.13	0.65 ± 0.10
QED	0.49 ± 0.22	0.51 ± 0.21	0.53 ± 0.18	0.52 ± 0.21	0.53 ± 0.21
RINGS	2.98 ± 1.42	2.52 ± 1.42	1.52 ± 0.98	2.68 ± 1.35	2.64 ± 1.43
AROMATIC RINGS	1.84 ± 1.31	1.12 ± 1.07	1.21 ± 0.95	1.52 ± 1.16	1.59 ± 1.22
HACCEPTORS	7.30 ± 4.49	6.19 ± 3.30	5.46 ± 2.21	6.67 ± 4.23	6.47 ± 3.64
HDONORS	2.62 ± 1.68	2.52 ± 1.65	1.55 ± 1.27	2.52 ± 1.68	2.66 ± 1.58
LOGP	0.29 ± 3.48	0.45 ± 3.08	-0.03 ± 2.33	0.29 ± 3.31	0.34 ± 2.99
MOLWT	390.43 ± 119.82	336.79 ± 107.86	337.30 ± 83.59	350.10 ± 114.00	336.09 ± 108.60
LIPINSKI	4.00 ± 1.34	4.45 ± 0.93	4.73 ± 0.55	4.35 ± 1.05	4.32 ± 1.05

Additionally, we compare FLOWR and PILOT in terms of drug-likeness filtering using the ‘Walters’-filter Walters et al. [1999], which evaluates generated compounds for unusual ring systems (by comparing their frequencies against ring systems found in ChEMBL) and identifies problematic functional groups through substructure matching against established filter collections, including Dundee, Glaxo, LINT, PAINS, BMS, and SureChEMBL. Fig. 14 (left) illustrates the performance comparison between FLOWR and PILOT based on these drug-likeness criteria. We observe that FLOWR consistently outperforms PILOT, in some cases by substantial margins, and generates compounds whose properties align more closely with those observed in the test set. Furthermore, Figure 14 (right) presents a comparative analysis of ring distributions, demonstrating that FLOWR again achieves significantly better overlap with the SPINDR test set distribution compared to PILOT.

D.2 Performance of FLOWR.MULTI on SPINDR

Here we report the evaluation results for FLOWR.MULTI using different conditional generation settings on the SPINDR test dataset. Tab.8 shows an overview of a set of evaluation metrics to assess pose quality and distribution learning capabilities.

D.3 4MPE: Visualizations

Here we show additional results on the protein target with PDB ID 4MPE for different conditional modes using the FLOWR.MULTI model. In Fig. 15 we provide the legend for the respective interaction diagrams.

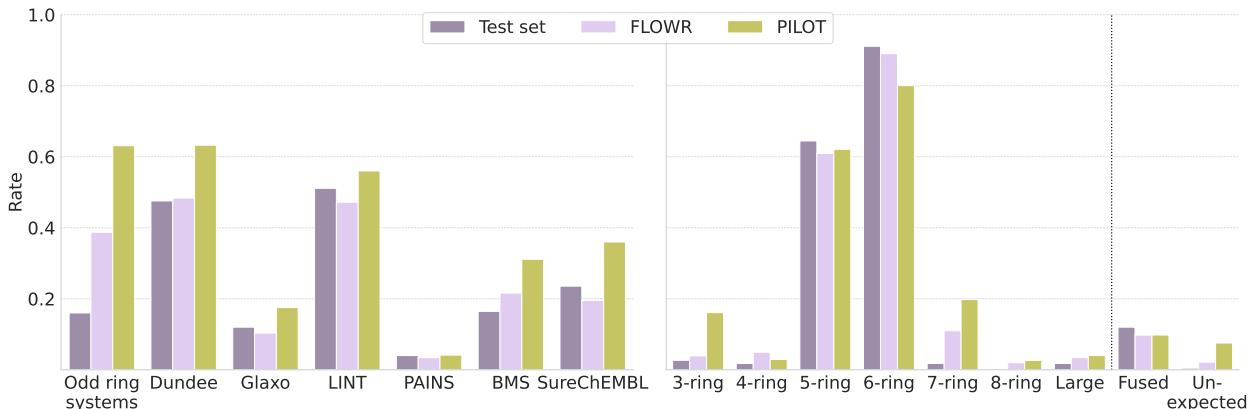


Figure 14: **Comparison of FLOWR and PILOT using the 'Walters'-filter and ring distribution analysis.** We assess the distribution learning capabilities of FLOWR and compare its performance against PILOT, utilizing established medicinal chemistry filters provided by the `USEFUL`RDKit`UTILS` toolkit (left panel). Specifically, we employed the REOS filter Walters et al. [1999] and the `RINGSYSTEMLOOKUP` to evaluate the generated ligands. Additionally, we present a comparative analysis of ring distributions (right panel). All reported metrics represent mean values computed from 100 ligands sampled per target using the SPINDR test dataset, which comprises 225 distinct test set targets. Ligand sizes were sampled uniformly around the ground truth ligand size, allowing for deviations within a range of $\pm 10\%$, using a consistent random seed across both models.

Table 8: We evaluate FLOWR.MULTI for different conditional modes, namely for interaction-, scaffold-, functional-group- and linker-conditional generation, on the SPINDR test set. We report RDKit- and PoseBusters-validity of generated ligands, the GenBench3D strain energy and the AutoDock-Vina score. We also state the pocket-ligand interaction fingerprint recovery rate and Tanimoto similarity using PROLIF, and the Wasserstein distance of generated ligands for the bond angles and bond lengths distribution to the SPINDR test set. Novelty, uniqueness and diversity measure the capability of the model to explore the chemical space both in 2D and 3D. RDKit’s QED evaluation, SAScore, the molecular weight as well as the logP values evaluate drug-likeness of generated ligands. All presented values are mean values taken for 100 sampled ligands per test set target. The test dataset comprises 225 test set targets. Ligand sizes were taken from the respective reference ligand and are not sampled. Note, both RDKit- and PoseBusters-validity values are evaluated on the generated set of 100 ligands per target. All other metrics are calculated on the subset of RDKit-valid ligands.

METRIC	FLOWR.MULTI ^{interact.-cond.}	FLOWR.MULTI ^{scaffold-cond.}	FLOWR.MULTI ^{f.-group-cond.}	FLOWR.MULTI ^{linker-cond.}
RDKit-VALIDITY	0.93 ± 0.25	0.93 ± 0.25	0.92 ± 0.26	0.92 ± 0.25
PB-VALIDITY	0.86 ± 0.19	0.88 ± 0.13	0.86 ± 0.17	0.85 ± 0.17
VINA SCORE	-7.18 ± 0.83	-7.41 ± 0.67	-7.10 ± 0.71	-7.35 ± 0.56
VINA SCORE (MINIMIZED)	-7.48 ± 0.80	-7.72 ± 0.59	-7.34 ± 0.72	-7.57 ± 0.56
STRAIN ENERGY	107.60 ± 93.07	86.26 ± 78.31	105.32 ± 95.47	94.56 ± 84.08
PLIF RECOVERY RATE	0.75 ± 0.08	0.65 ± 0.11	0.79 ± 0.12	0.79 ± 0.08
PLIF TANIMOTO SIMILARITY	0.66 ± 0.09	0.62 ± 0.10	0.74 ± 0.13	0.76 ± 0.09
BONDANGLESW1	1.17	0.84	1.14	0.91
BONDLENGTHSW1 [10 ⁻²]	0.43	0.52	0.58	0.69
NOVELTY	0.93 ± 0.26	0.94 ± 0.23	0.87 ± 0.33	0.87 ± 0.33
UNIQUENESS2D	0.83 ± 0.26	0.74 ± 0.28	0.70 ± 0.33	0.53 ± 0.31
UNIQUENESS3D	0.40 ± 0.21	0.35 ± 0.12	0.31 ± 0.20	0.26 ± 0.17
DIVERSITY2D	0.82 ± 0.08	0.77 ± 0.07	0.78 ± 0.08	0.75 ± 0.06
DIVERSITY3D	0.06 ± 0.07	0.02 ± 0.01	0.07 ± 0.12	0.03 ± 0.05

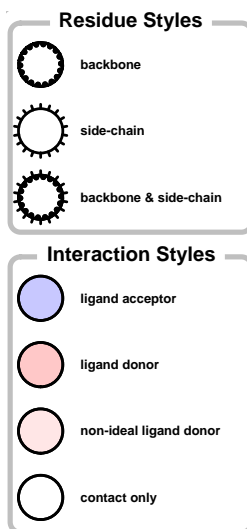


Figure 15: Legend for interaction visualizations on 4MPE

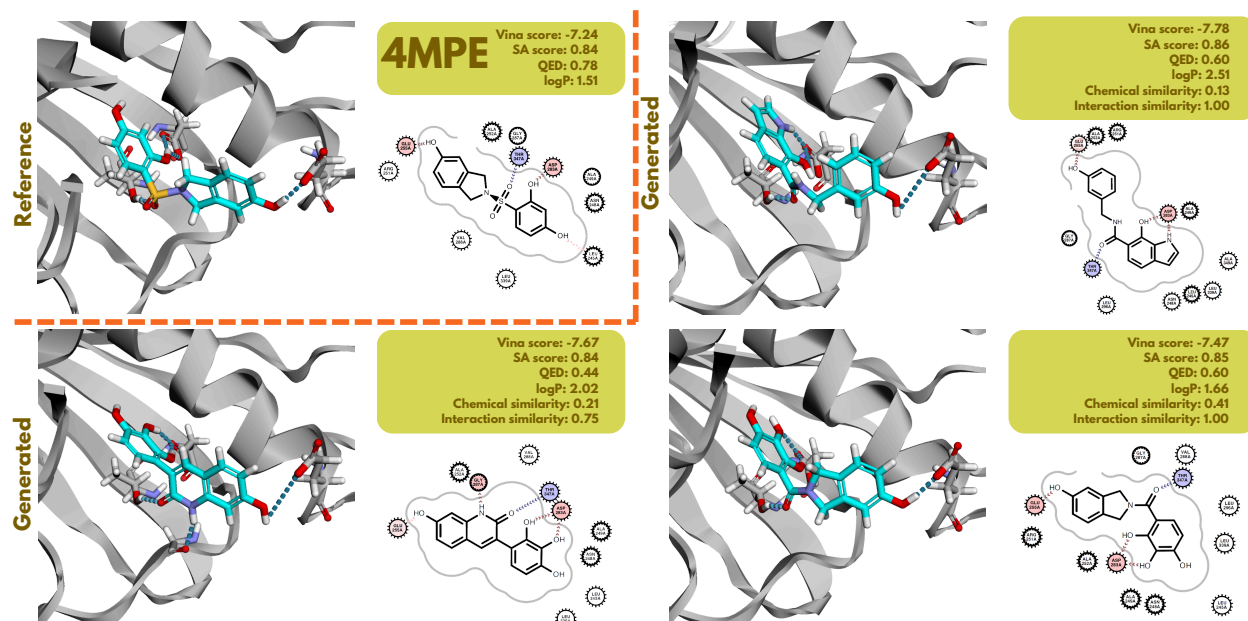


Figure 16: **Evaluation of interaction-conditional generation on 4MPE with FLOWR.MULTI** Using the interaction-conditional generation mode of FLOWR.MULTI, we sample 100 ligands for a randomly selected target from the SPINDR test set, here 4MPE. We then select three ligands at random and compare them to the reference compound based on Vina score, SA score, QED, logP, chemical similarity, and interaction similarity.

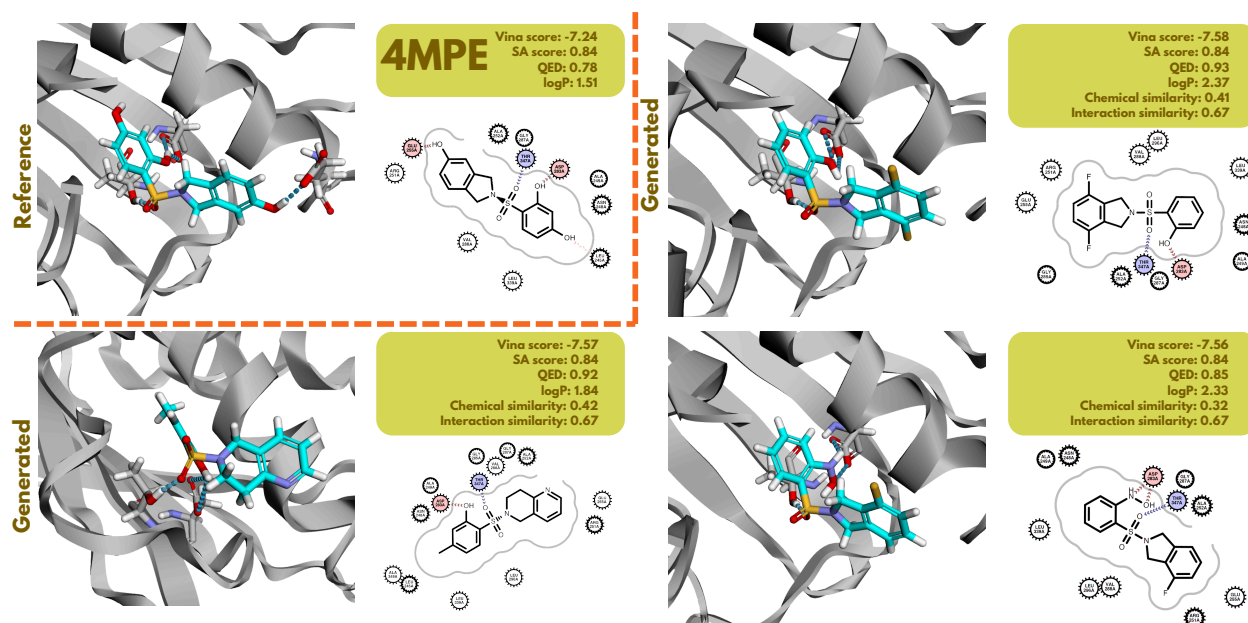


Figure 17: **Evaluation of scaffold-conditional generation on 4MPE with FLOWR.MULTI** Using the scaffold-conditional generation mode of FLOWR.MULTI, we sample 100 ligands for a randomly selected target from the SPINDR test set, here 4MPE. We then select three ligands at random and compare them to the reference compound based on Vina score, SA score, QED, logP, chemical similarity, and interaction similarity.

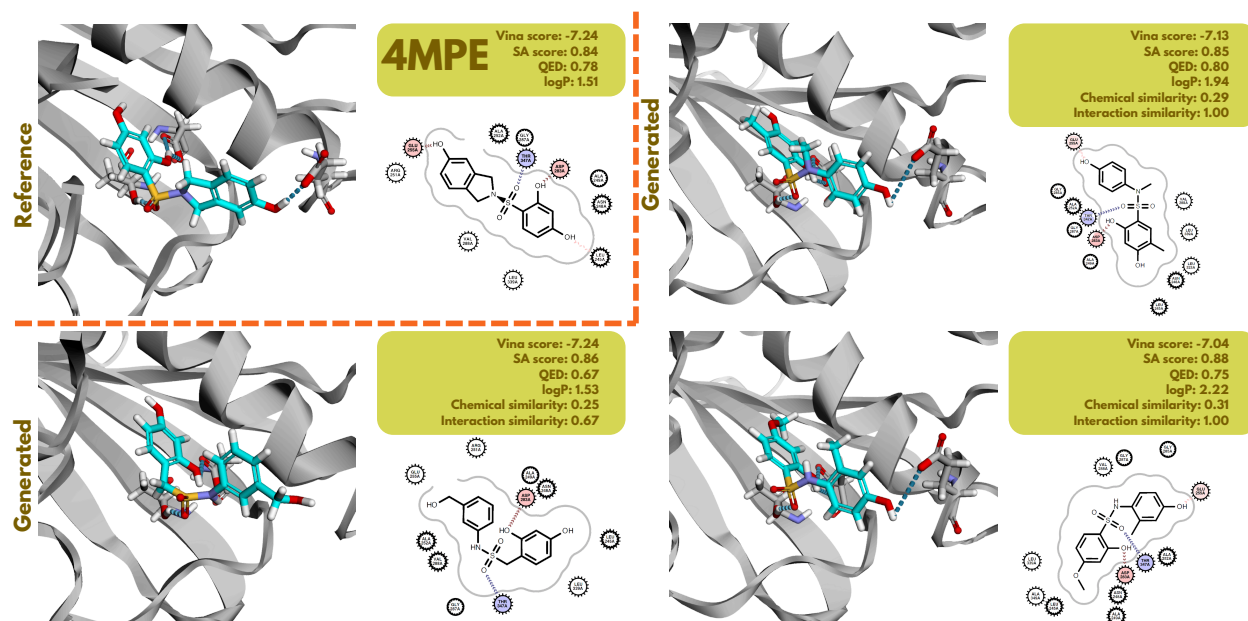


Figure 18: **Evaluation of functional-group-conditional generation on 4MPE with FLOWR.MULTI** Using the functional-group-conditional generation mode of FLOWR.MULTI, we sample 100 ligands for a randomly selected target from the SPINDR test set, here 4MPE. We then select three ligands at random and compare them to the reference compound based on Vina score, SA score, QED, logP, chemical similarity, and interaction similarity.

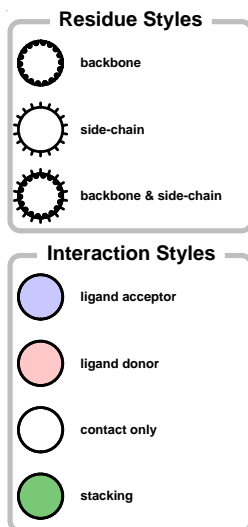


Figure 19: Legend for interaction visualizations on 5YEA

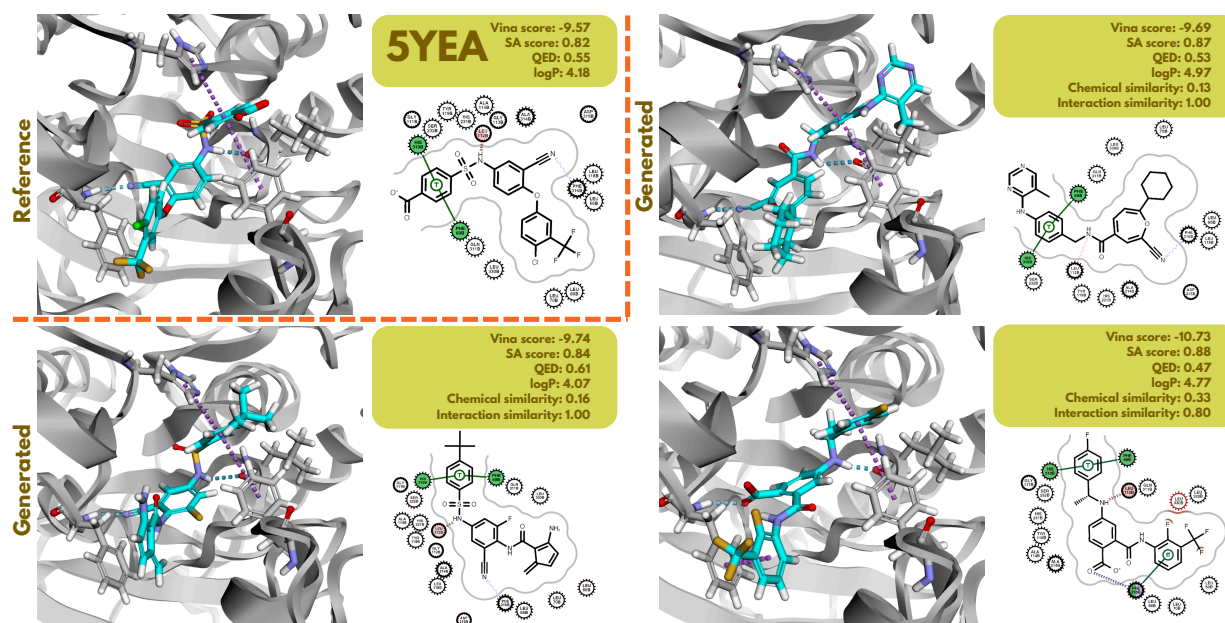


Figure 20: **Evaluation of interaction-conditional generation on 5YEA with FLOWR.MULTI** Using the interaction-conditional generation mode of FLOWR.MULTI, we sample 100 ligands for a randomly selected target from the SPINDR test set, here 5YEA. We then select three ligands at random and compare them to the reference compound based on Vina score, SA score, QED, logP, chemical similarity, and interaction similarity.

D.4 5YEA: Visualizations

Here we show additional results on the protein target with PDB ID 5YEA for different conditional modes using FLOWR.MULTI. In Fig. 19 we provide the legend for the respective interaction diagrams.

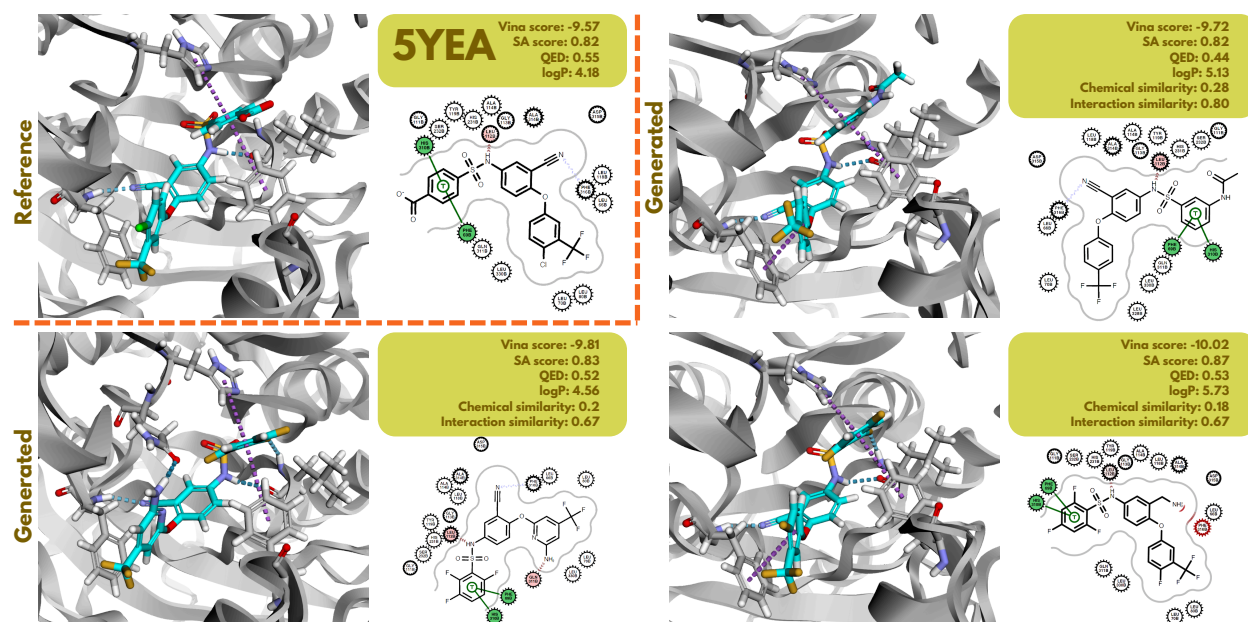


Figure 21: **Evaluation of scaffold-conditional generation on 5YEA with FLOWR.MULTI** Using the scaffold-conditional generation mode of FLOWR.MULTI, we sample 100 ligands for a randomly selected target from the SPINDR test set, here 5YEA. We then select three ligands at random and compare them to the reference compound based on Vina score, SA score, QED, logP, chemical similarity, and interaction similarity.

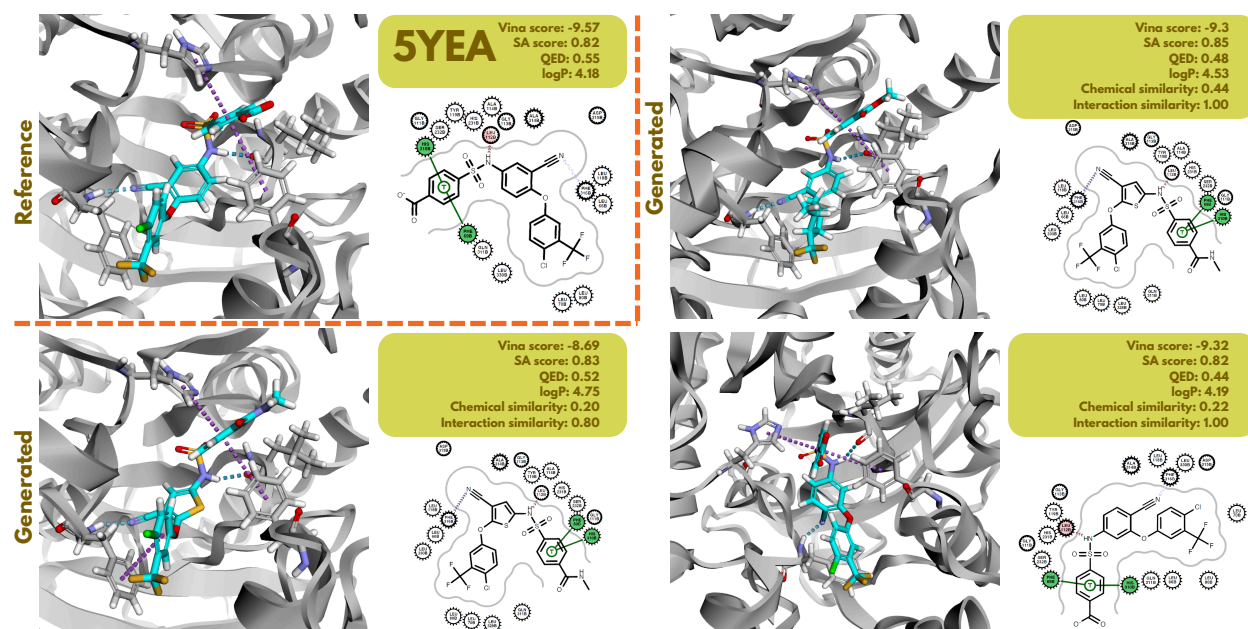


Figure 22: **Evaluation of functional-group-conditional generation on 5YEA with FLOWR.MULTI** Using the functional-group-conditional generation mode of FLOWR.MULTI, we sample 100 ligands for a randomly selected target from the SPINDR test set, here 5YEA. We then select three ligands at random and compare them to the reference compound based on Vina score, SA score, QED, logP, chemical similarity, and interaction similarity.